



# The Complex Star Formation History of the Halo of NGC 5128 (Cen A)

Sima T. Aghdam<sup>1</sup>, Atefeh Javadi<sup>1</sup> , Seyedazim Hashemi<sup>2,3</sup>, Mahdi Abdollahi<sup>1</sup>, Jacco Th. van Loon<sup>4</sup> , Habib Khosroshahi<sup>1</sup>,  
Roya H. Golshan<sup>5</sup> , Elham Saremi<sup>1,6,7</sup> , and Maryam Saberi<sup>8</sup>

<sup>1</sup> School of Astronomy, Institute for Research in Fundamental Sciences (IPM), Tehran 19568-36613, Iran; [atefeh@ipm.ir](mailto:atefeh@ipm.ir)

<sup>2</sup> Department of Physics and Astronomy, University of California, Riverside, Riverside, CA 92521, USA

<sup>3</sup> Department of Physics, Sharif University of Technology, Tehran 11155-9161, Iran

<sup>4</sup> Lennard-Jones Laboratories, Keele University, Keele ST5 5BG, UK

<sup>5</sup> I. Physikalisches Institut, Universität zu Köln, Zùlpicher Straße 77, 50937 Cologne, Germany

<sup>6</sup> Instituto de Astrofísica de Canarias, Universidad de La Laguna, C/ Via Láctea s/n, 38205 La Laguna, Tenerife, Spain

<sup>7</sup> Departamento de Astrofísica, Universidad de La Laguna, 38205 La Laguna, Tenerife, Spain

<sup>8</sup> Rosseland Centre for Solar Physics, University of Oslo, P.O. Box 1029, Blindern, NO-0315 Oslo, Norway

Received 2022 December 1; revised 2024 May 23; accepted 2024 May 31; published 2024 August 23

## Abstract

NGC 5128 (Cen A) is the nearest giant elliptical galaxy and one of the brightest extragalactic radio sources in the sky, boasting a prominent dust lane and jets emanating from its nuclear supermassive black hole. In this paper, we construct the star formation history (SFH) of two small fields in the halo of NGC 5128: a northeastern field (Field 1) at a projected distance of  $\sim 18.8$  kpc from the center, and a southern field (Field 2)  $\sim 9.9$  kpc from the center. Our method is based on identifying long-period variable (LPV) stars that trace their sibling stellar population and hence historical star formation due to their high luminosity and strong variability; we identified 395 LPV stars in Field 1 and 671 LPV stars in Field 2. Even though the two fields are  $\sim 28$  kpc apart on opposite sides from the center, they show similar SFHs. In Field 1, the star formation rate (SFR) increased significantly around  $t \sim 800$  Myr and  $t \sim 3.8$  Gyr and in Field 2, the SFR increased considerably around  $t \sim 800$  Myr,  $t \sim 3.8$  Gyr, and  $t \sim 6.3$  Gyr, where  $t$  is the lookback time. The increase in SFR  $\sim 800$  Myr ago agrees with previous suggestions that the galaxy experienced a merger around that time. The SFH reconstructed from LPV stars supports a scenario in which multiple episodes of nuclear activity lead to episodic jet-induced star formation. While there is no catalog of LPV stars for the central part of NGC 5128, applying our method to the outer regions (for the first time in a galaxy outside the Local Group) has enabled us to put constraints on the complex evolution of this cornerstone galaxy.

*Unified Astronomy Thesaurus concepts:* Galaxy jets (601); Late stellar evolution (911); Star formation (1569); Galaxy evolution (594); Asymptotic giant branch stars (2100)

*Materials only available in the [online version of record](#): figure set, machine-readable table*

## 1. Introduction

Considering our location in the Local Group (LG), we have a great opportunity to study resolved populations of spiral galaxies and obtain more knowledge about their formation and evolution. However, there is no giant elliptical (GE) galaxy in the LG, therefore, our understanding is limited to the nearest elliptical galaxies in the other groups. NGC 5128 (aka Centaurus A, or Cen A), with a distance of 3.8 Mpc ( $\mu = 27.87 \pm 0.16$  mag, Rejkuba et al. 2004a;  $E(B - V) = 0.15 \pm 0.05$  mag, Rejkuba et al. 2001) offers us a unique opportunity to study the nearest GE galaxy up close (Harris et al. 1999; Charmandaris et al. 2000; Rejkuba 2004b; Rejkuba et al. 2005), which is located in the Centaurus group of galaxies (Karachentsev 2005).

There is some doubt about the galaxy type of NGC 5128. It has been classed as a GE galaxy based on its optical light distribution (Baade & Minkowski 1954; Graham 1979). Other studies have suggested that it is an SO-type galaxy based on the dust lane and lenticular morphology (Morgan 1958; van den Bergh 1990). On balance, though, NGC 5128 is generally considered as a GE galaxy (Harris 2010).

NGC 5128's extended halo and radio lobes cover almost  $2^\circ$  of the sky (Peng et al. 2002) in optical maps. In recent years, the halo of NGC 5128 has been the subject of intense scrutiny (e.g., Crnojević et al. 2014; Rejkuba et al. 2014; Neff et al. 2015; Crnojević et al. 2016; Salomé et al. 2016a, 2016b; D'Souza & Bell 2018; Hernandez et al. 2018). NGC 5128 is believed to be a postmerger galaxy (Peng et al. 2002), one of only a handful of halos resolved into individual stars (Rejkuba et al. 2011). The stellar streams and field stars in the halo can be used to trace the signature of mergers and/or interactions. Moreover, an active galactic nucleus (AGN) at the center of NGC 5128 produces the nearest example of powerful radio jets (Crockett et al. 2012). AGN activity and its effect on the regulation of the star formation and evolution of the host galaxy is an important yet still open question in galaxy formation and evolution theory (e.g., Ciotti & Ostriker 1997; Silk & Rees 1998; Binney 2004; Silk 2005; Springel et al. 2005; Schawinski et al. 2007; Sijacki et al. 2007).

The star formation history (SFH) is a crucial component of galaxy formation and evolution. Recovering the SFH in resolved galaxies is typically based on the color–magnitude diagrams (CMDs) of individual stars where the signatures of different stellar populations can be traced (e.g., Tolstoy & Saha 1996; Holtzman et al. 1999; Olsen 1999; Dolphin 2002; Javadi et al. 2011b). This type of analysis is confined to a few dozen galaxies that mostly lie within our LG because of the



Original content from this work may be used under the terms of the [Creative Commons Attribution 4.0 licence](#). Any further distribution of this work must maintain attribution to the author(s) and the title of the work, journal citation and DOI.

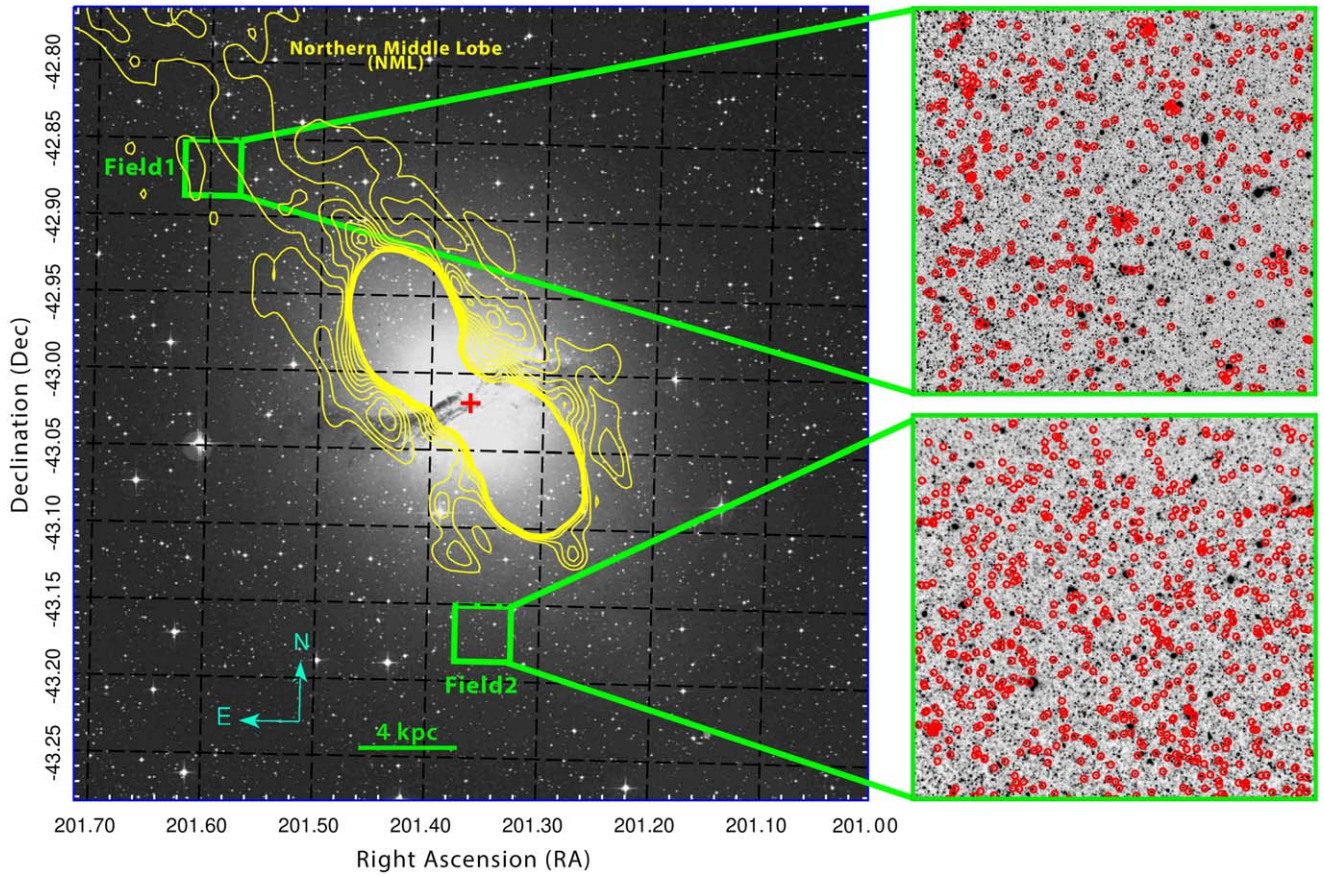


**Figure 1.** Archival optical image (at 468 nm wavelength) of NGC 5128 taken with the UK Schmidt Telescope overlaid with the location of the fields studied here (each one is about  $2\frac{2}{3} \times 2\frac{2}{3}$ ) (left). The red cross indicates the center of NGC 5128 (Ma et al. 1998). Red circles represent the locations of the selected LPV stars from the ISAAC Ks-band data. The yellow overlay contours are the radio emission that show the structure of the lobes at 1392 and 128 MHz presented in Morganti et al. (1999). The northern middle lobe (NML) is located in the upper left of the figure, while the north and south lobes are located in the north and south of the galaxy.

limited spatial resolution (within  $\sim 2$  Mpc; Ruiz-Lara et al. 2015).

In this work, we aim to find the SFH of two small fields in the halo of NGC 5128 using long-period variable (LPV) stars in order to understand the relation between the SFH of the halo and its merger history. Large-amplitude ( $>10\%$  or so) regular or semiregular LPV stars are cool evolved stars spanning a wide age range from  $\sim 10$  Myr to  $\sim 10$  Gyr. These stars are very luminous,  $\sim 1000$ – $500,000 L_{\odot}$ , in proportion to their birth mass, and of low temperature ( $T \sim 2500$ – $4500$  K); hence they are the most accessible tracers of stellar populations (e.g., Maraston 2005; Maraston et al. 2006; Javadi et al. 2011a, 2011b, 2013, 2015). LPV stars are mostly evolved asymptotic giant branch (AGB) stars of  $\gtrsim 30$  Myr (e.g., Fraser et al. 2005, 2008; Soszyński et al. 2009) varying on timescales of  $\approx 100$ – $1300$  days, making them easily identifiable (Javadi et al. 2011b, 2011c, 2015, 2017; Rezaei et al. 2014; Hamedani Golshan et al. 2017; Hashemi et al. 2019; Navabi et al. 2021; Saremi et al. 2020, 2021). Recent star formation ( $\sim 10$ – $30$  Myr) can be traced in a similar way by red supergiants (RSGs) with birth masses  $\sim 8$ – $30 M_{\odot}$ . AGB stars inject up to 80% of their mass into the interstellar medium (ISM) and play a significant role in the chemical enrichment of the galaxy; mass loss can, in some cases, also be important for RSGs and their fate as supernovae (Vassiliadis & Wood 1993; Javadi et al. 2013; van Loon et al. 1999, 2005).

This paper is structured as follows. In Section 2, the data used for the study are presented. There is a short explanation

about the detected LPV stars in Section 3. A discussion of removing the contaminating stars can be found in Section 4. The metallicity of the galaxy is discussed in Section 5. We provide a brief description of the method used for studying its SFH in Section 6. Section 7 derives the SFHs of two fields in NGC 5128, and to obtain accurate star formation rates (SFRs), we identify a probability function to simulate the nondetected LPV stars in Section 8. This is followed by discussion and a summary in Sections 9 and 10, respectively.

## 2. Data

We used near-infrared photometry obtained with ISAAC at the ESO Paranal UT1 Antu 8.2 m Very Large Telescope in two different fields in the halo of NGC 5128. These data were published by Rejkuba et al. (2001) and analyzed by Rejkuba et al. (2003a). In addition, we also used near-infrared photometry obtained with SOFI at the ESO La Silla 3.5 m New Technology Telescope for Field 2. Figure 1 presents an optical image of NGC 5128 taken with the UK Schmidt Telescope (Ma et al. 1998) overlaid by Field 1 and Field 2 that are studied in this work. It should be noted that Field 1 and Field 2 are the same as the fields studied in Rejkuba et al. (2003a) but smaller than the ones mentioned in Rejkuba et al. (2001).

Field 1 is centered at  $\alpha = 13^{\text{h}} 26^{\text{m}} 23^{\text{s}}.5$ ,  $\delta = -42^{\circ} 52' 0''$  on the eminent northeastern part of the halo, at a distance of  $\sim 17'$



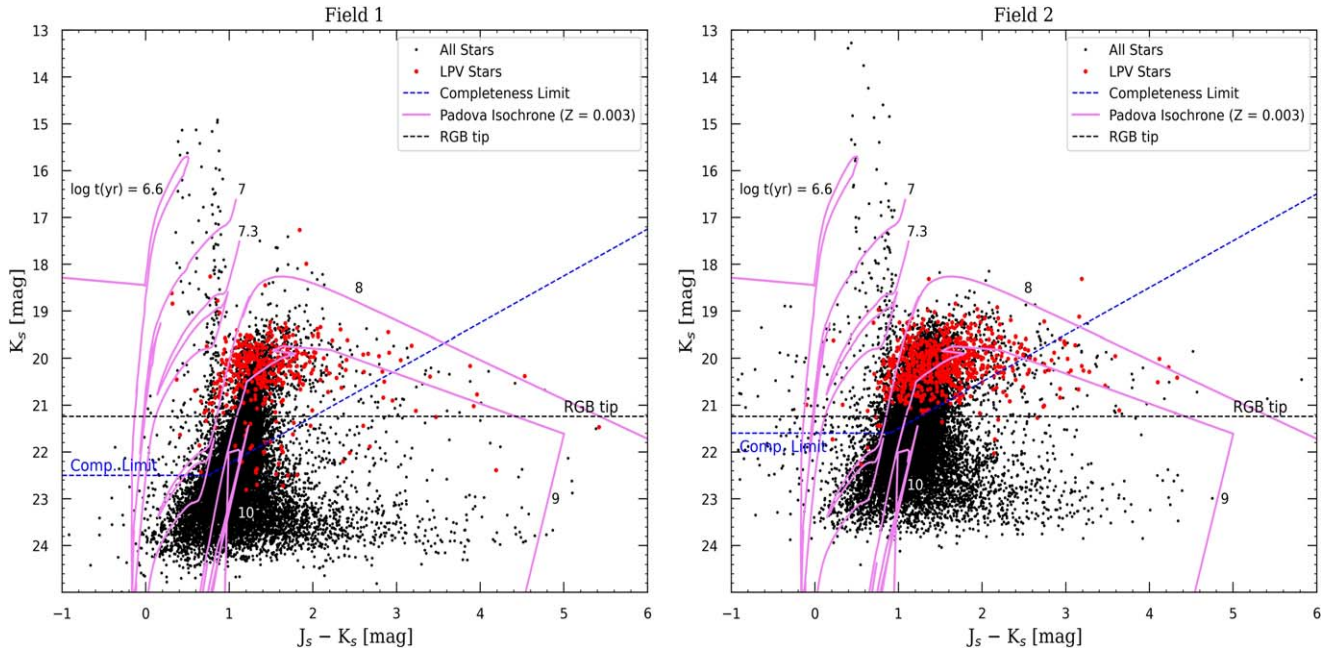


**Figure 2.**  $K_s$  vs.  $J_s - K_s$  CMD for the stars with at least three  $K_s$ -band detections (black dots) and LPV stars (red dots) in Field 1 (left) and Field 2 (right). The black and blue dotted lines represent the RGB tip and completeness limit magnitudes, respectively, in each field (Rejkuba et al. 2003a). The purple lines show theoretical stellar isochrones for a metallicity  $Z = 0.003$  for six different ages (Marigo et al. 2017).

**Table 1**

Summary of the Data Taken from Rejkuba et al. (2001), Rejkuba et al. (2003a), and Rejkuba et al. (2003b) as Used in This Paper

Field	R.A. (J2000)	Decl. (J2000)	Distance to Center arcmin (kpc)	Coverage arcmin <sup>2</sup> (kpc <sup>2</sup> )	Number		Completeness Limit (mag)	RGB Tip (mag)
					Total	LPV		
Field 1	13 <sup>h</sup> 26 <sup>m</sup> 23 <sup>s</sup> .5	−42° 52′ 0″	~17 (18.8)	~5.2 (5.7)	15,574	437	50% at $K_s = 22.5$	$K_s = 21.24$
Field 2	13 <sup>h</sup> 25 <sup>m</sup> 26 <sup>s</sup> .0	−43° 10′ 0″	~9 (9.9)	~5.2 (5.7)	18,098	709	50% at $K_s = 21.5$	$K_s = 21.24$

(~18.8 kpc), far from the center of the galaxy, with a dimension of  $2'28 \times 2'30$  (5.7 kpc<sup>2</sup>).

Field 1 is placed on the so-called inner filaments discovered by Morganti et al. (1991). The filaments, along the direction of the northern radio jet, are extended from ~13 to ~22 kpc (Salomé et al. 2016b) and contain ionized gas, young star clusters, and ultraviolet emission (Neff et al. 2015). Young stars are  $\lesssim 10$  Myr old (e.g., Mould et al. 2000; Crockett et al. 2012), thus indicating recent and ongoing star formation (e.g., Rejkuba et al. 2004a; Neff et al. 2015). The filaments and their star formation are suggested to be the result of interactions between jets and gas (e.g., Charmandaris et al. 2000; Auld et al. 2012; Crockett et al. 2012; Santoro et al. 2015a; Santoro et al. 2015b; Salomé et al. 2016b).

Field 2 is centered at  $\alpha = 13^h 25^m 26^s$ ,  $\delta = -43^\circ 10' 0''$  at a distance of  $\sim 9'$  ( $\sim 9.9$  kpc) from the center, with a dimension of  $2'25 \times 2'31$  (5.7 kpc<sup>2</sup>).

### 3. Long-period Variable Stars in NGC 5128

To identify LPV stars, Rejkuba et al. (2003a) performed multipoch photometry in the  $K_s$  band, along with single-epoch photometry in the  $J_s$  and  $H$  bands. The 50% completeness limit in  $K_s$  and  $H$  is 22.5 mag in Field 1 and 21.5 mag in Field 2. As a result, 15,574 and 18,098 sources in Field 1 and Field 2 are detected, respectively, with at least three  $K_s$ -band observations, among which more than 1500 variable stars are identified. Based on a Fourier analysis, Rejkuba et al. (2003a) could

determine periods and amplitudes for 1046 red variables with at least 10  $K_s$ -band measurements. Among them, 437 and 709 LPV stars are detected in Field 1 and Field 2, respectively, most of which are brighter than the tip of the red giant branch (RGB; Rejkuba et al. 2003b).

Our selected sample to estimate the SFHs includes all identified LPV stars with periods longer than 70 days (from Rejkuba et al. 2003a). Considering these criteria, we have 395 and 671 LPV stars in Field 1 and Field 2, respectively. On the right side of Figure 1 the distribution of selected LPV stars (red circles) in their fields is depicted.

Figure 2 shows  $K_s$  versus  $J_s - K_s$  CMDs for all those detected in at least three  $K_s$  bands. The RGB tip is at  $K_s = 21.24$  mag; the completeness limits are  $K_s = 22.5$  mag and  $K_s = 21.5$  mag in Field 1 and Field 2, respectively (Rejkuba et al. 2003a). Rejkuba et al. (2003b) found that it is necessary to subtract 0.1 mag from the originally published  $K_s$ -band magnitudes. A summary of the data used in this paper is presented in Table 1.

### 4. Contamination

The observations of NGC 5128 ( $l = 309^\circ 515$ ,  $b = +19^\circ 417$ ) are probably contaminated by foreground stars from the Milky Way. The contamination level can be determined by cross-matching our catalog with the recently published Gaia Early Data Release 3 (Brown et al. 2021). The completeness limit of

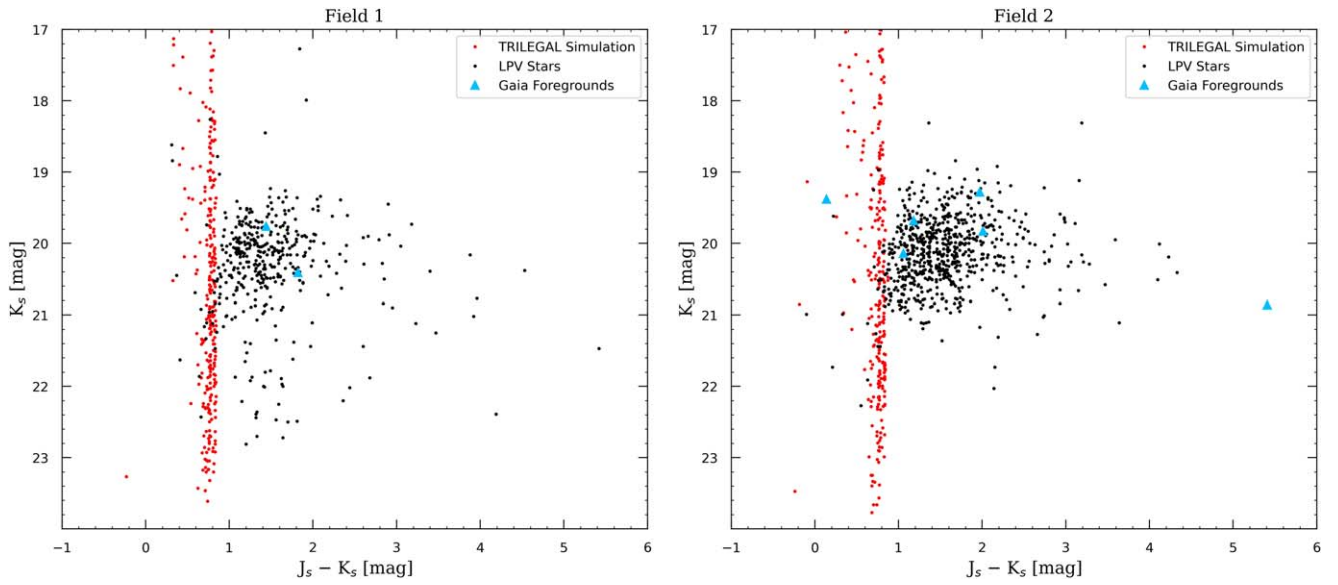


**Figure 3.** The obtained contamination of Field 1, left panel, and Field 2 right panel. Black dots represent detected LPV stars. Red dots show the TRILEGAL simulation of the  $0.002 \text{ deg}^2$  area, indicating low levels of contamination. Blue triangles are crossmatched with the Gaia catalog; we found only eight stars to be foreground, two of which are in Field 1 and six in Field 2.

Gaia is  $G \approx 19\text{--}21$  mag, meaning that 50% of stars are brighter than  $G \sim 20$  mag (Brown et al. 2021).

Stars were considered as foreground objects if they satisfied one of the following criteria as explained in detail by Saremi et al. (2020): (a) the star’s proper motion is consistent with the relation  $\sqrt{\mu_{\text{R.A.}}^2 + \mu_{\text{decl.}}^2} > 0.28 + 2 \text{ error mas yr}^{-1}$  (van der Marel et al. 2019) or (b) the ratio of the parallax to its error is larger than  $2\sigma$ . We note that increasing the threshold from two to five did not affect the selection results. Thus, eight foreground stars were found, of which two were in Field 1 and six in Field 2.

To verify the level of contamination, we simulated the foreground population using the TRILEGAL stellar population synthesis code (Girardi et al. 2005) via its web interface. We assumed two areas of  $0.002 \text{ deg}^2$  in the directions of Field 1 and Field 2. The results of these simulations along with the detected LPV stars in the two fields are shown in Figure 3, indicating that the color of the simulated data is  $J_s - K_s < 0.9$  mag, while the LPV stars have a redder color. Therefore, there is no significant contamination between the Milky Way and the detected LPV stars.

### 5. Metallicity of the Halo of NGC 5128

With age, because of nucleosynthesis and the chemical enrichment of the galaxy by old and dying stars, the metallicity at various locations within the galaxy changes. In general, it is expected that older stars formed in a metal-poor environment while younger stars formed in a metal-rich one (Vassiliadis & Wood 1993; van Loon et al. 1999; Javadi et al. 2011a). The CMDs of Figure 2, specifically the evolved branch stars, reveal that the main chemical enrichment of the galaxy occurred 3 Gyr ago.

The metallicity matters when reconstructing the SFH. A large number of globular clusters (GCs) was studied spectroscopically by Woodley et al. (2010), yielding a metallicity range  $-1.7 \lesssim [\text{M}/\text{H}] \lesssim 0.4$  dex ( $0.0003 \lesssim Z \lesssim 0.05$ ). The majority of the halo was covered by their study, including

Field 1 and Field 2. Their results are in agreement with Rejkuba et al. (2011), who found  $0.0001 < Z < 0.04$  by comparing an observed CMD obtained with the Hubble Space Telescope (HST) of a field in the halo of NGC 5128 (located 38 kpc south of the center) with simulated CMDs. While this region is far from the ones we present here, they exhibit a similar range of metallicity. Considering these results and other works by Peng et al. (2004), Beasley et al. (2008), and Rejkuba et al. (2001), we adopt the metallicity range  $0.0003 < Z < 0.04$  for both fields.

### 6. Method

The method we used to calculate the SFHs is based on LPV stars and was developed by Javadi et al. (2011b), which has since been applied in a variety of studies (Javadi et al. 2011b, 2011c, 2017; Rezaei et al. 2014; Hamedani Golshan et al. 2017; Hashemi et al. 2019; Navabi et al. 2021; Saremi et al. 2021). We estimated birth mass, age, and LPV phase duration (the duration that stars are in the LPV phase) of LPV stars by applying Padova evolutionary models (Marigo et al. 2017) and assuming a range of constant metallicities. The stellar mass is estimated by the mass–luminosity relation, and the mass–age relation gives the age of stars. The LPV phase duration can be investigated using the mass–LPV phase duration relation of the star as detailed in the Appendix. Finally, LPV stars are sorted according to their ages and divided into bins. The SFR for different bins with specified intervals in age and mass can be calculated using:

$$\xi(t) = \frac{dn'(t)}{\delta t} \frac{\int_{\min}^{\max} f_{\text{IMF}}(m) m \, dm}{\int_{m(t)}^{m(t+dt)} f_{\text{IMF}}(m) \, dm}, \quad (1)$$

where  $m$  is the birth mass,  $f_{\text{IMF}}(m)$  is the Kroupa initial mass function (IMF) defined as  $f_{\text{IMF}} = A m^{-\alpha}$  where  $A$  is the normalization coefficient, which is canceled out here, and  $\alpha$

depends on the mass range, following Kroupa (2001):

$$\alpha = \begin{cases} +0.3 \pm 0.7 & \text{for } \min \leq m/M_{\odot} < 0.08, \\ +1.3 \pm 0.5 & \text{for } 0.08 \leq m/M_{\odot} < 0.50, \\ +2.3 \pm 0.3 & \text{for } 0.50 \leq m/M_{\odot} < \max. \end{cases} \quad (2)$$

The minimum and maximum of the stellar mass range are adopted to be 0.02 and 200  $M_{\odot}$ , respectively. Reasonable adjustments to these values are unlikely to cause the SFR to vary by more than a factor of 2.  $dn'$  is the amount of observed LPV stars in each bin, and  $\delta t$  is the LPV phase duration.

The statistical error bars for each bin are calculated using a Poisson distribution:

$$\sigma_{\xi(t)} = \frac{\sqrt{N}}{N} \xi(t), \quad (3)$$

where  $N$  is the number of stars in each age bin.

To estimate SFHs in this paper, we assumed 11 metallicities to cover the metallicity of very old ( $\gtrsim 12$  Gyr) to very young ( $\sim 1$  Gyr) populations in the galaxy ( $0.0003 < Z < 0.04$ ; Rejkuba et al. 2005, 2011; Woodley et al. 2010). The fitted lines/curves and corresponding equations for obtaining the mass, age, and LPV phase duration of LPV stars are presented in the Appendix for all metallicities, with details of the fitting and related plots. We aimed to use the latest version of the Padova evolutionary model (Marigo et al. 2017); however, the final version fails to consider the variability of massive stars, but there are some stars in the halo of NGC 5128 younger than 100 Myr. Thus, we used the older release of Marigo et al. (2008) for the LPV phase duration of massive stars ( $\log(M/M_{\odot}) > 0.8$ ).

LPV stars in the AGB (or RSG) phase produce dust, which attenuates their light. This effect depends on wavelength, resulting in reddening of the near-infrared colors (Vassiliadis & Wood 1993; van Loon et al. 1999, 2005; Javadi et al. 2011b). To obtain the intrinsic  $Ks$ -band magnitudes, we need to apply a dereddening process. To correct for circumstellar extinction, we plot a CMD of the LPV stars and theoretical isochrones by Marigo et al. (2017). The slope of the isochrones is related to dust regardless of whether it is oxygenous or carbonaceous in its composition. We expect the stars with a  $1.5 < M/M_{\odot} < 4$  birth mass to have become carbon stars due to the carbon-to-oxygen ratio  $> 1$  in the third dredge-up of nuclear-processed material, but in a low-metallicity environment a lower limit of 1.1  $M_{\odot}$  is considered (Leisenring et al. 2008). In addition, for stars with  $M/M_{\odot} < 1.1$ , the third dredge-up has not occurred sufficiently, and for stars with  $M/M_{\odot} > 4$  nuclear burning of the carbon at the bottom of the convection zone prevents the carbon from enriching the surface; hence these stars are oxygen-rich stars. Therefore, it is understood that the reddening of carbon stars differs from oxygen stars. Having corrected the  $Ks$ -band magnitudes and separated oxygenous and carbonaceous stars, the birth mass will be calculated assuming the maximum  $Ks$ -band brightness achieved by the stellar models.

### 6.1. How to Calculate the Star Formation Rate

The approach we use to derive the SFHs from the LPV star catalog is outlined as follows.

1. LPV stars have achieved peak brightness in near-infrared wavelengths, allowing us to estimate their mass using stellar evolution models. Additionally, being in the

advanced stages of their evolution, their mass can be translated into age (stellar lifetime). As a result, the identification of LPV stars through comprehensive long-term monitoring surveys is imperative, forming the foundation for subsequent mass and age estimations. Once LPV stars are identified, it is crucial to account for two corrections in the analysis. First, due to the potential incompleteness inherent in monitoring surveys, a simulated fraction of potentially missed LPV stars needs to be reintegrated into the list. This correction, detailed in Section 8 following Rejkuba et al. (2003a)'s simulations, takes into consideration various parameters such as magnitude range, period, and amplitude. Consequently, a formula has been developed to quantify this incompleteness. Second, the influence of circumstellar dust must be addressed. The bending of isochrones after their peak indicates the presence of circumstellar dust, leading to the dimming and reddening of LPV stars. Our methodology for determining stellar mass and age assumes that stars are at the pinnacle of their isochrones. To account for this, dereddening equations derived from isochrones slopes are employed to correct the magnitudes and restore them to their optimal states. Correcting for circumstellar reddening requires observations in at least two bands, enabling estimation of the star's color. Hence the correction equation is:

$$K_0 = K_s + a(1.5 - (J_s - K_s)), \quad (4)$$

where  $K_0$  is the corrected magnitude,  $a$  is the slope of the isochrone,  $K_s$  and  $J_s - K_s$  are the observed magnitude and color of each LPV star, respectively. This correction is applied to variable stars with  $J_s - K_s > 1.5$  mag.

2. In the subsequent phase, we employ Padova stellar evolutionary models to determine the peak of the isochrones (in the  $K_s$  band) across a range of different ages. Following this, we establish a correlation between the mass of stars associated with these peaks and their luminosity (Table 9). As mentioned earlier, the LPV stars are positioned at the zenith of the isochrones (following correction for circumstellar dust). Therefore, this relationship will provide a mass estimation for each LPV star. Then the age of each LPV star is estimated using the mass–age relationship, taking into account that LPV stars represent the endpoint of stellar evolution (Table 10). Utilizing the age–metallicity relationship (AMR) specific to each galaxy, we establish these correlations for diverse metallicities. Consequently, for each star, both mass and age can be estimated across all available choices of metallicity. To better understand this method, consider a star in the CMD (Figure 2) with  $K_s \sim 20$  mag and  $J_s - K_s \sim 1$  mag. While the isochrones suggest that this star aligns well with the 100 Myr isochrone, our method assumes that as an LPV, this star must be at the peak of the isochrone. Therefore, we cannot allocate this star to the 100 Myr isochrone because its brightness is much fainter than what the 100 Myr isochrone suggests at its peak. Instead, its magnitude suggests that this star aligns well with the peak of the isochrone at  $\log t = 9.32$ . As we know, photometric errors may cause stars to appear redder or bluer than their actual colors, making it challenging to align the star with each isochrone. However, since our method is not CMD based and only uses one filter to estimate mass and age, the effect of



photometric errors is negligible in the final results (see Section 8.1).

We must mention an important uncertainty in the Padova models regarding the evolution of super-AGB stars, which have birth masses in the range of approximately  $5\text{--}10 M_{\odot}$  (Siess 2007). These models do not compute the entire thermal-pulsing phase of super-AGB stars, causing their evolution to appear to terminate prematurely. This uncertainty is evident as an excursion toward fainter  $Ks$ -band magnitudes in Figure 17 for the range of  $0.7 < \log(M/M_{\odot}) < 1 - 1.1$ . To address this, we interpolate the mass–luminosity relation over this mass range, providing a continuous connection between the final luminosities of AGB stars and those of massive RSGs.

3. An aspect of significant importance concerning the presentation of a SFH is the way it is binned in terms of age. The younger, more massive variable stars are often considerably fewer than the older, low-mass variable stars, and inadequate binning can either lead to spurious peaks in the SFR or mask any such real bursts. From a statistical point of view, an advantage lies in ensuring that each bin contains the same number of stars, thus providing uniform uncertainties to the SFR values. To accomplish this, we initiated the process by arranging stars by mass and began counting until a predetermined number was reached. At that point, we commenced counting stars for the subsequent bin. Through this approach, it becomes evident that each bin is associated with a specific mass range, supposing stars with masses between  $m(t)$  and  $m(t + dt)$  are within one of these bins. Our methodology assumes that all stars within this mass range should now be identified as LPV stars. However, due to statistical limitations (ensuring an adequate number of stars in each bin), the age bin ( $dt$ ) associated with that mass bin is larger than the LPV phase duration ( $\delta t$ ). In this case, if a star with mass  $m(t + dt)$ —currently identified as an LPV—formed later in that bin, it will not be recognized as an LPV since it has not yet reached the LPV phase when we currently observe it. A similar situation also applies to the lowest-mass limit in that bin: if stars with mass  $m(t)$ , currently identified as LPV stars, had formed slightly earlier (beyond the LPV phase duration of those stars) within that same bin, they would not be identified as LPV stars because they would have already completed this phase. These are just examples, but the same logic applies to all stars formed within that age bin.

To clarify, let us consider that we want to calculate the SFH between  $\log t = 8.98\text{--}9.08$ . During this period, our ability to identify stars is limited to those with masses between 2 and  $2.2 M_{\odot}$  because they have reached their final evolutionary stage and can be identified as LPV stars. For example, consider a star with a mass of  $2 M_{\odot}$  which formed  $t \sim 1.20$  Gyr ago ( $\log t = 9.08$ ) and has presently entered the LPV phase. This star remains at this evolutionary stage for  $\delta t \sim 2.4$  Myr ( $\log \delta t = 6.38$ ), making it recognizable as an LPV. Therefore, since this star will remain in this phase for 2.4 Myr, if it forms 2.4 Myr later, it can still be recognized as an LPV. However, if its formation occurred outside this timeframe, exceeding the  $\delta t$  from the beginning of this age bin, it has

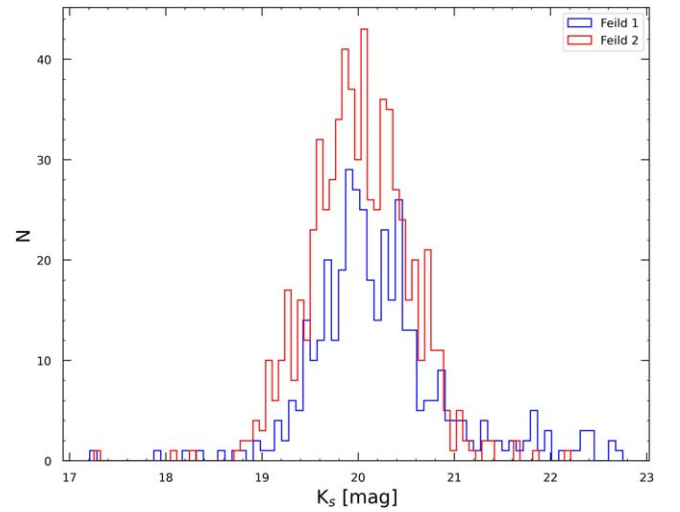


**Figure 4.**  $Ks$ -band luminosity function for LPV stars. The circumstellar dust correction is applied to stars with  $J_s - K_s > 1.5$  mag.

not yet reached the final evolutionary stage and will not be identified as an LPV. For the mentioned example, the age bin is almost 250 Myr, several times longer than the LPV phase duration. Hence, we cannot identify all stars formed within this specific mass range because some have not entered the LPV phase yet, or have just finished the phase. This fraction is influenced by the duration of the age bin ( $dt$ ) and the LPV phase duration ( $\delta t$ ) of each star. Therefore, the proportion of recognized LPV stars in that bin compared to the overall count of stars formed within the range of  $m(t + dt)$  and  $m(t)$  in the same bin is equivalent to  $\frac{\delta t}{dt}$ .

To address this consideration in our analysis, we developed a relationship between LPV phase duration and mass (Table 11). This value serves as a weight for each star, as depicted in Equation (1). Essentially, the inverse of the LPV phase duration for each star is estimated and then aggregated over the specific bin. Finally, we apply the IMF correction based on the minimum and maximum mass of each bin. Substituting these parameters into Equation (1) yields the SFR within that specific bin. The luminosity function of LPV stars after applying the circumstellar dust correction for stars with  $J_s - K_s > 1.5$  mag is illustrated in Figure 4. Our method involves considering the number of LPV stars across different magnitude ranges. However, it is crucial to note that two corrections are applied to the LPV star counts. The first correction accounts for LPV phase duration, while the second one involves applying the IMF. Consequently, the  $Ks$ -band histogram does not track the SFH (Figure 13), as expected.

4. Finally, we present the SFH in two formats. First, as shown in Figure 5, we display various SFHs, each corresponding to a constant metallicity. It is evident that due to the galaxy’s chemical enrichment, the highest metallicity suitable for recent times is not suitable for older epochs. However, the advantage of this representation lies in the fact that, guided by AMRs, the appropriate SFR value for each bin can be selected. These SFHs can be further consolidated into a single graph based on the assumed AMRs, as depicted in Figure 13. It must be

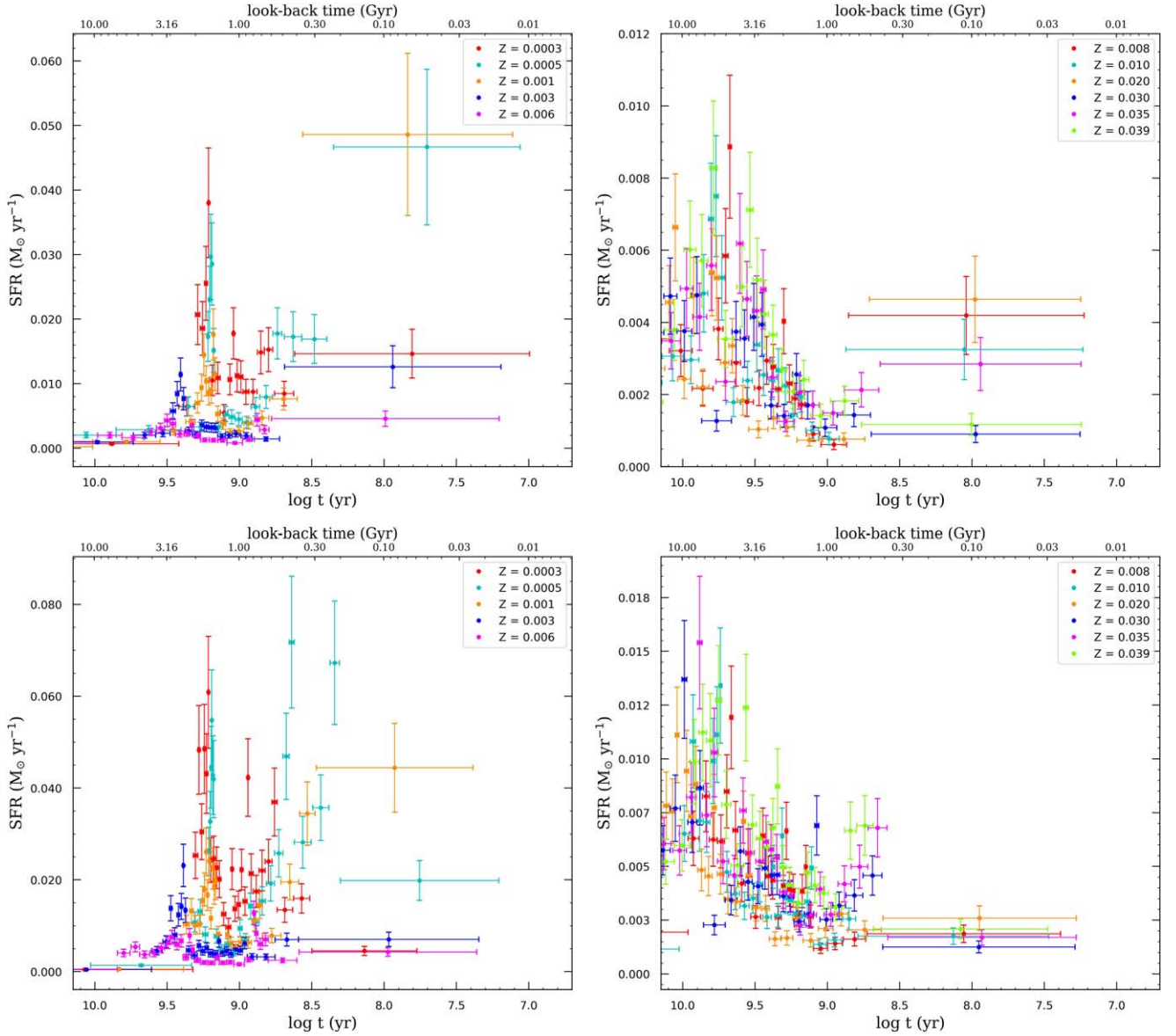


**Figure 5.** Calculated SFHs for different metallicities for Field 1 (upper panel) and Field 2 (lower panel). The sample includes 395 and 671 LPV stars with periods longer than 70 days for Fields 1 and 2, respectively.

noted that while these SFHs can be useful for estimating the SFR in specific age bins based on the appropriate metallicity of those age bins, complications arise when age bins encompass two or more metallicity ranges, making it challenging to estimate the exact SFR. For example, in the Woodley model (see Section 8.6),  $Z=0.003$  is appropriate for the age bin  $\log t \sim 9.90\text{--}10.08$ . However, in the presented SFHs, the SFR for this metallicity is calculated for the age bin  $\log t \sim 9.70\text{--}10.20$ , which spans age bins suitable for different metallicities. To address this, instead of directly utilizing these SFHs, we derived all the necessary relationships required in Equation (1) to construct the SFH, taking into consideration the AMRs. For instance, to establish the  $K_s$  band–age relationship, we utilized the appropriate metallicity for each age bin as outlined in Tables 7 and 8. Isochrones at the corresponding metallicity for each age duration were utilized to estimate

the peak of the isochrone in the  $K_s$  band. Finally, lines were fitted to the data points to derive metallicity-dependent age–luminosity relationships, as illustrated in Figure 12.

## 7. Results

Having considered our sample (Sections 2 and 3) and having applied the method (Section 6), we calculated the SFR in each epoch for different metallicities based on a function of age in the galaxy. The number of stars selected in each bin is a crucial parameter. On the one hand, large numbers of stars in a bin may cause the age interval to be wider and not reveal variation within the bin. In contrast, small numbers of stars per bin can cause confusing and meaningless fluctuations.

As we expect the results to be sensitive to the metallicity, the difference between the actual and calculated SFR in each epoch depends on the difference between the actual and assumed

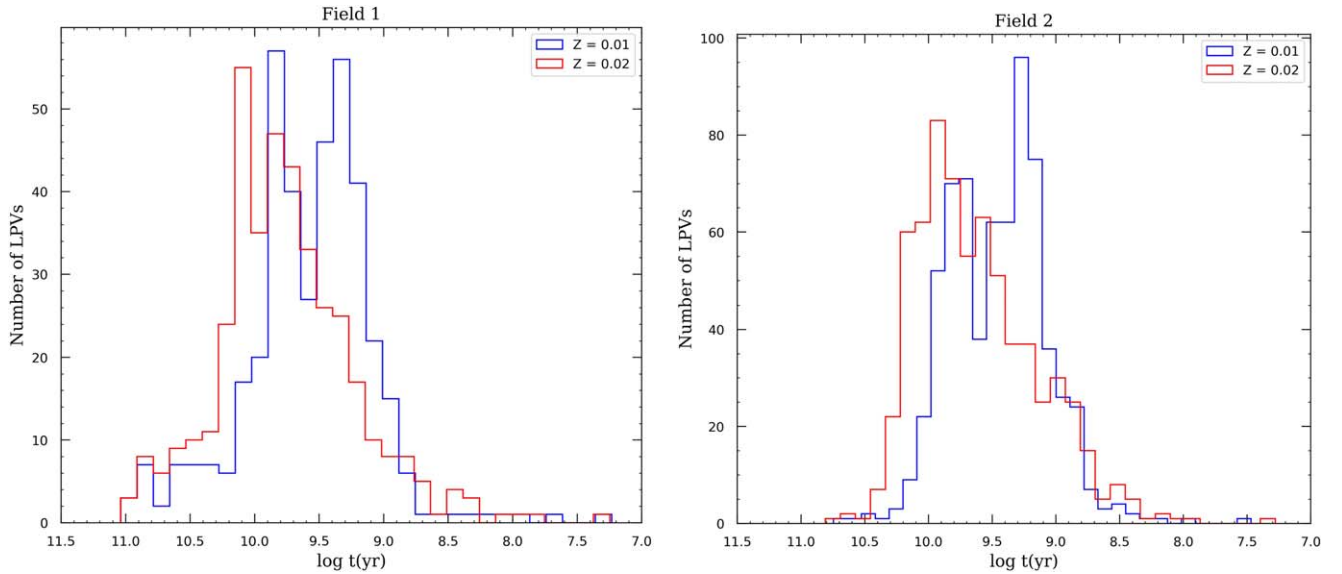


**Figure 6.** Age histogram of LPV stars for two metallicities ( $Z = 0.01$  and  $Z = 0.02$ ) in Field 1 and Field 2, where  $t$  is the lookback time.

metallicity for the epoch. To trace the change of metallicity over time, we use different metallicities corresponding to stellar populations of different ages. The effect of metallicity on SFR arises when we calculate the mass, age, and LPV phase duration of each star, which are explained in the [Appendix](#). Figure 5 shows there is a significant difference in the derived SFRs using different metallicities. The oldest bin is only partially displayed as it stretches to unrealistically large ages. It is included in the plot solely to illustrate that, as anticipated, the SFR we calculate for ages exceeding the Hubble time is negligible for the metallicity range suitable for these epochs (Figure 5, left panel). However, as depicted in the right panel of Figure 5, for higher metallicities, this value is not negligible. Nevertheless, based on the AMRs for this galaxy (see Section 8.6), these metallicities are not suitable for the oldest bins; hence, the values derived based on them are not reliable.

The calculated SFRs of Field 1 and Field 2 for several constant metallicities are presented in Figure 5. As can be seen, applying different (but constant in time) metallicities results in very similar SFR patterns (SFR variations in time) for both fields. While one field is in the northeastern part (Field 1) and the other in the south (Field 2),  $\sim 28$  kpc apart, they show very similar SFHs. On the other hand, Field 2 experienced a higher SFR at all ages likely due to its location closer to the center of the galaxy.

For low to intermediate metallicities in the range  $0.0003 \leq Z \leq 0.006$  in both Field 1 and Field 2, we do not recover stellar populations older than  $\log t(\text{yr}) \gtrsim 9.8$  but do find a consistent pattern of two peaks in SFR, one at  $\log t(\text{yr}) \sim 9.3\text{--}9.6$  and another at  $\log t(\text{yr}) \sim 8.6\text{--}9.0$  (both older for higher metallicity)—the latter coincides with a major merger  $t \sim 800$  Myr ago (Israel 1998). For higher metallicities in the range  $0.008 \leq Z \leq 0.039$ , on the other hand, a significant population of older stars is recovered, with a peak in star formation around  $\log t(\text{yr}) \sim 9.8\text{--}10$  ( $t \sim 8\text{--}10$  Gyr)—such old stars were also reported by Kaviraj et al. (2005), Rejkuba et al. (2005), and Woodley et al. (2010), and we suggest here that they be relatively metal rich. Also in this metallicity range a hike in SFR is seen to occur  $t \sim 800$  Myr ago.

Woodley et al. (2010) studied 72 GCs in the halo of NGC 5128 and noted that more than 85% of these are old and

metal poor. Some of them, though, with an age of 10 Gyr, have metallicities  $Z > 0.008$ . From Figure 6, it is clear that most of the stars in the halo of NGC 5128 are older than 1 Gyr, which is also in agreement with their results.

Rejkuba et al. (2004a) investigated recent star formation in NGC 5128 by simulating a  $U\text{--}V$  CMD of a field that encompassed Field 1. For two metallicities,  $Z = 0.004$  and  $Z = 0.008$ , changing the slope of the Salpeter IMF and the starting and ending epochs of star formation, they found that the SFRs 100 Myr ago are in the range of  $\sim 9 \times 10^{-5}$  to  $\sim 10^{-3} M_{\odot} \text{ yr}^{-1} \text{ kpc}^{-2}$ . Assuming metallicities of  $Z = 0.003$  and  $Z = 0.008$  for Field 1 ( $5.7 \text{ kpc}^2$ ), we derive  $\text{SFR} = 2.2 \times 10^{-3} M_{\odot} \text{ yr}^{-1} \text{ kpc}^{-2}$  and  $\text{SFR} = 9.7 \times 10^{-4} M_{\odot} \text{ yr}^{-1} \text{ kpc}^{-2}$ , respectively, for  $\log t(\text{yr}) \leq 8.7$ , which seems reasonable since they mentioned that their results are lower than what they had expected for a GE galaxy.

Figure 6 presents LPV star age histograms for two metallicities,  $Z = 0.01$  and  $Z = 0.02$ , for both fields. It highlights the presence of a distinct star formation epoch around  $\log t(\text{yr}) \sim 9.3$  at subsolar metallicity, which however disappears if the populations have solar metallicity.

## 8. Accounting for Observational Bias

### 8.1. Photometric Uncertainties

In this section, we investigate the impact of accounting for photometric uncertainties on the derived SFH. Our method is not based on CMD studies; instead, it focuses on the brightness of stars in the  $K_s$  band. When we consider the error in magnitude, the star's brightness undergoes slight variations, resulting in a corresponding adjustment in its assigned mass (and consequently, its age).

Figure 7 illustrates the SFH for  $Z = 0.008$  when we incorporate photometric errors in the  $K_s$  band from the mean magnitude. Overall, we observe a similar behavior in the SFH with comparable epochs of star formation as seen when using the mean magnitude (Tables 5 and 6). However, it is not surprising to find that the SFH shifts toward earlier or later epochs when we add or subtract photometric errors.



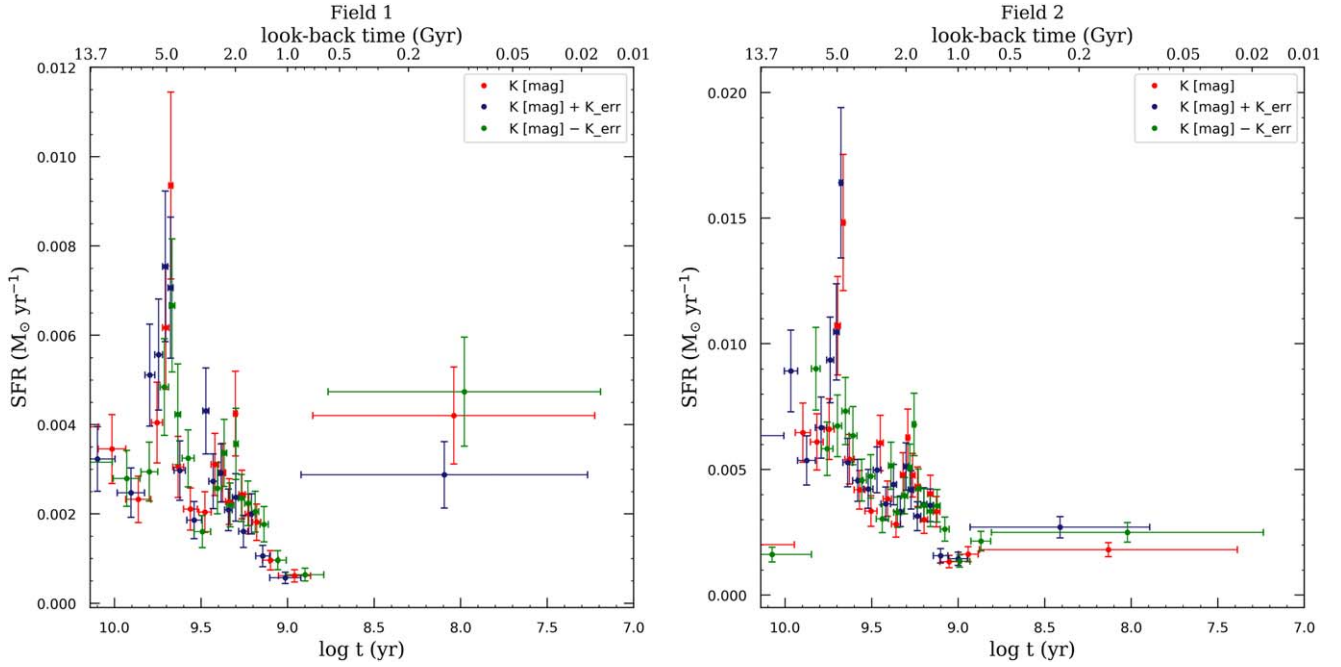


**Figure 7.** SFHs derived by considering the photometric errors for Field 1 (left panel) and Field 2 (right panel) at  $Z = 0.008$ .

Nevertheless, the overall effect of these errors on the SFH is negligible.

Given our focus on LPV stars, whose brightness typically exceeds that of the RGB tip in surveys deep enough to cover RGB stars, photometric errors for LPV stars are generally lower (mostly less than 0.1 mag). As mentioned, our method does not rely on CMD-based studies and solely utilizes LPV star brightness to estimate mass and age. Consequently, photometric errors cannot lead to stars being associated with the wrong isochrone, a common challenge encountered in CMD-based studies. This highlights a strength of our approach. For example, consider an LPV star with  $K_s = 21$  mag. The models suggest that this star should have a mass of  $0.95 M_\odot$  and an age of 10.8 Gyr (at  $Z = 0.008$ ). Accounting for a photometric error of 0.1 mag in the  $K_s$  band, the mass varies between  $0.91$  and  $0.99 M_\odot$  and the age varies between 9.5 and 12.4 Gyr ( $\log t = 9.97$ – $10.09$ ). Notably, the width of the age bins used to derive the star formation during these times is  $\log dt \sim 0.2$  (see Figure 7), significantly larger than the age shift caused by accounting for photometric errors.

## 8.2. Comparison with BaSTI Models

It is important to emphasize that our method relies on model predictions, and among the available models, the Padova models are the only ones providing essential information about pulsation behavior, a key component of our approach. While there are other models that simulate the thermal-pulsing AGB evolution (such as the BaSTI models by Pietrinferni et al. 2004, 2021) these models do not cover super-AGB stars like the Padova models.

Here we compare the mass–luminosity and mass–age relations between the BaSTI and Padova models (Figure 8). The main difference is that the faintest stars, around  $\sim -7.63$  mag, are less massive and older when using the BaSTI models ( $\sim 9.9$  Gyr compared to 3.8 Gyr when using the Padova

models), but the difference is negligible for intermediate-age stars (about 1 Gyr old). Additionally, as can be seen in the right panel of Figure 8, the BaSTI models do not cover the mass range of RSGs, which is important when deriving the recent SFH from our method.

As indicated in Equation (1), one of the parameters necessary for deriving the SFH is the LPV phase duration of LPV stars ( $\delta t$ ). This parameter is essential for converting the count of identified LPV stars to the SFR. However, BaSTI models do not provide any estimation of  $\delta t$ , hence we cannot derive the SFH using the BaSTI models.

## 8.3. Simulated Data and the Probability Function

NGC 5128 is a distant galaxy, hence it is unlikely we have detected all of its LPV stars. The likelihood for an LPV to be identified depends on its mean brightness, period, and amplitude. Finding this probability is a key point in the method since the number of detected LPV stars directly affects the SFH results.

To determine the completeness limit, Rejkuba et al. (2003a) simulated LPV stars and compared them with their catalog for  $K_s < 20.5$  mag and  $K_s > 20.5$  mag separately. Their simulated variable stars span a magnitude range of  $19.5 < K_s < 21.5$ , with  $K_s$ -band amplitudes between 0.1 and 1.4 mag for two constant periods of 100 and 450 days, and for an amplitude of  $\Delta K_s = 0.7$  mag for periods from 50 to 1100 days.

To find the multidimensional probability function, we used the simulation results from Rejkuba et al. (2003a; detailed information is presented in Appendix A.2). The first part is a period–probability diagram for  $\Delta K_s = 0.7$  mag, while the next parts are amplitude–probability diagrams for  $P = 100$  and  $P = 450$  days. We now need to determine a function that maintains the dependence on period and amplitude since they will affect each other. The cross terms are expected to satisfy the condition since this is what makes

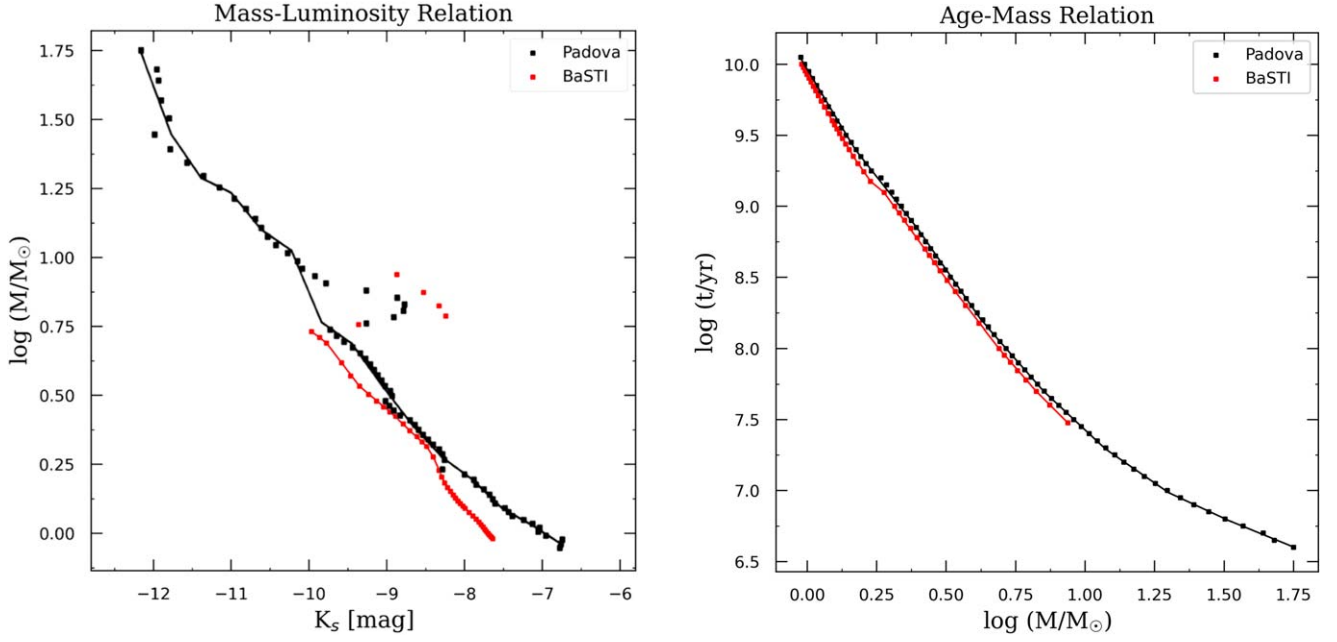


**Figure 8.** The mass–luminosity (left panel) and mass–age (right panel) relations are depicted, considering Padova models (black line) and BaSTI models (red line) at  $Z = 0.008$ .

statistical sense. By using functions for  $f(A)$  and  $f(P)$ , we obtain  $f(A, P) = f(A) \times f(P)$ .

The shape of the period–probability diagram (Rejkuba et al. 2003a Figures 12 and 14) suggests the need for a high-order polynomial function, while the amplitude function might be represented by an error function—it has both the statistical significance and the functional shape we need. The error function (also called the Gaussian error function),  $\text{erf}$ , is a complex function of a complex variable:

$$\text{erf } z = \frac{2}{\sqrt{\pi}} \int_0^z e^{-t^2} dt. \quad (5)$$

It is not possible to fit the integral form of  $\text{erf}$  to the data. Instead, we use an approximation (Abramowitz & Stegun 1972):

$$\begin{aligned} \text{erf } A = 1 - & \left[ \alpha_1 \left( \frac{1}{1 + \beta A} \right) + \alpha_2 \left( \frac{1}{1 + \beta A} \right)^2 \right. \\ & \left. + \alpha_3 \left( \frac{1}{1 + \beta A} \right)^3 \right] e^{-A^2}. \end{aligned} \quad (6)$$

We thus find two functions: Equation (7), valid for  $K_s > 20.5$  mag, and Equation (8), valid for  $K_s < 20.5$  mag, whose coefficients are presented in Tables 2 and 3, respectively. Figure 9 illustrates the accuracy of the fitting function on the data belonging to Field 1 for  $K_s < 20.5$  mag—see Appendix A.2 for the other fits. We must note that the probability of bright stars exceeds 100%. There are two critical reasons assigned by Rejkuba et al. (2003a). The first one is about the moving of some faint stars into brighter magnitude bins (Malmquist bias). The second one is related to false detection or migration, which happens because of blending

**Table 2**  
Coefficients of the Probability Function of Field 1 and Field 2 for Simulated Variable Stars of  $K_s > 20.5$  mag, Related to Equation (7)

$N$	Symbol	Coefficient: Field 1	Coefficient: Field 2
1	$\alpha_1$	$-1.305 \times 10^2$	$-3.782 \times 10^3$
2	$\alpha_2$	$-96.808$	$-2.639 \times 10^3$
3	$\alpha_3$	$2.385 \times 10^2$	$6.424 \times 10^3$
4	$\beta$	$0.322$	$6.483 \times 10^{-4}$
5	$\eta$	$2.008$	$1.935$
6	$\gamma_1$	$8.166 \times 10^{-2}$	$7.553 \times 10^{-1}$
7	$\gamma_2$	$-7.452 \times 10^{-4}$	$-7.021 \times 10^{-3}$
8	$\gamma_3$	$3.344 \times 10^{-6}$	$3.006 \times 10^{-5}$
9	$\gamma_4$	$-7.911 \times 10^{-9}$	$-6.722 \times 10^{-8}$
10	$\gamma_5$	$9.873 \times 10^{-12}$	$8.036 \times 10^{-11}$
11	$\gamma_6$	$-6.133 \times 10^{-15}$	$-4.868 \times 10^{-14}$
12	$\gamma_7$	$1.493 \times 10^{-18}$	$1.174 \times 10^{-17}$
13	$\delta_1$	$3.588 \times 10^5$	$-1.592 \times 10^5$
14	$\delta_2$	$-2.256 \times 10^7$	$1.034 \times 10^7$
15	$\delta_3$	$1.000$	$1.000$
16	$\delta_4$	$2.038 \times 10^3$	$1.106 \times 10^3$

with original stars in the images.

$$\begin{aligned} f(A, P) = & \left( 1 - \left[ \alpha_1 \left( \frac{1}{1 + \beta A} \right) + \alpha_2 \left( \frac{1}{1 + \beta A} \right)^2 \right. \right. \\ & \left. \left. + \alpha_3 \left( \frac{1}{1 + \beta A} \right)^3 \right] e^{-\eta A^2} \right) \times (\gamma_1 P + \gamma_2 P^2 + \gamma_3 P^3 + \gamma_4 P^4 \\ & + \gamma_5 P^5 + \gamma_6 P^6 + \gamma_7 P^7) + \delta_1 \frac{A^2}{P^2} + \delta_2 \frac{A^3}{P^3} \\ & + \delta_3 \frac{A^4}{P^4} + \delta_4 \frac{A^2}{P}, \end{aligned} \quad (7)$$

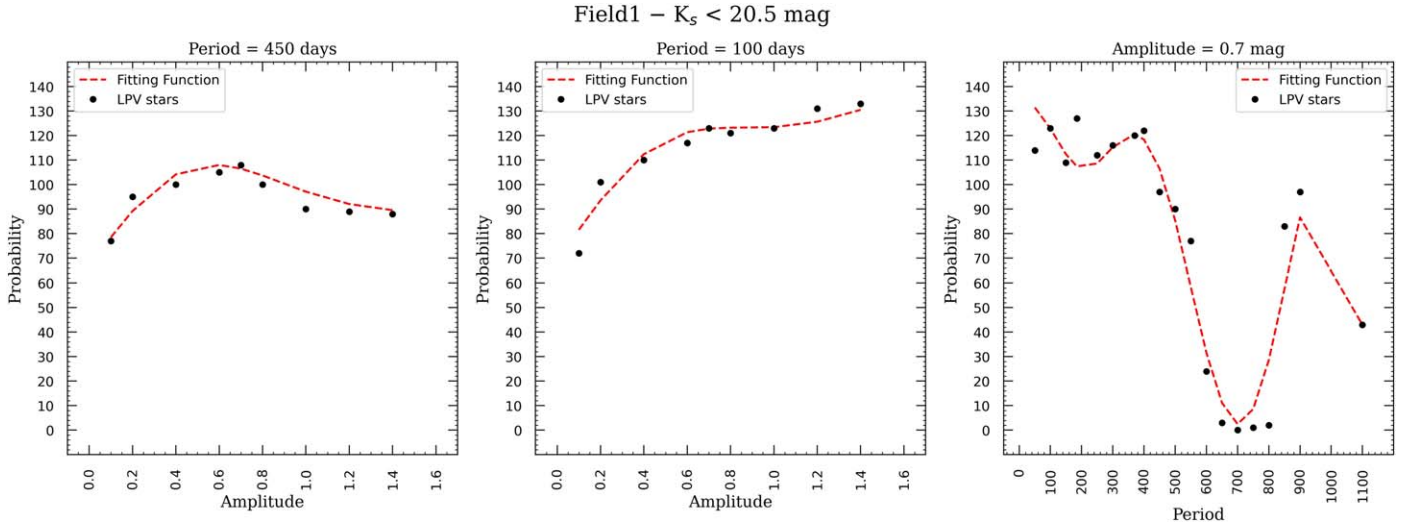


**Figure 9.** The result of fitting a probability function to the data with  $K_s < 20.5$  mag in Field 1. More details are presented in Appendix A.2.

**Table 3**

Coefficients of the Probability Function of Field 1 and Field 2 for Simulated Variable Stars of  $K_s < 20.5$  mag, Related to Equation (8)

$N$	Symbol	Coefficient: Field 1	Coefficient: Field 2
1	$\alpha_1$	-37.589	$6.004 \times 10^{-1}$
2	$\alpha_2$	-29.358	-1.414
3	$\alpha_3$	67.154	2.561
4	$\beta$	$1.276 \times 10^{-2}$	3.817
5	$\eta$	2.122	$5.385 \times 10^{-2}$
6	$\gamma_1$	2.432	4.144
7	$\gamma_2$	$-2.497 \times 10^{-2}$	$-4.522 \times 10^{-2}$
8	$\gamma_3$	$1.197 \times 10^{-4}$	$2.204 \times 10^{-4}$
9	$\gamma_4$	$-2.927 \times 10^{-7}$	$-5.411 \times 10^{-7}$
10	$\gamma_5$	$3.721 \times 10^{-10}$	$6.936 \times 10^{-10}$
11	$\gamma_6$	$-2.338 \times 10^{-13}$	$-4.432 \times 10^{-13}$
12	$\gamma_7$	$5.740 \times 10^{-17}$	$1.114 \times 10^{-16}$
13	$\delta_1$	$3.359 \times 10^5$	$2.456 \times 10^4$
14	$\delta_2$	$-9.117 \times 10^6$	$3.267 \times 10^6$
15	$\delta_3$	1.000	1.000

$$\begin{aligned}
 f(A, P) = & \left( 1 - \left[ \alpha_1 \left( \frac{1}{1 + \beta A} \right) + \alpha_2 \left( \frac{1}{1 + \beta A} \right)^2 \right. \right. \\
 & \left. \left. + \alpha_3 \left( \frac{1}{1 + \beta A} \right)^3 \right] e^{-\eta A^2} \right) \times (\gamma_1 P + \gamma_2 P^2 + \gamma_3 P^3 + \gamma_4 P^4 \\
 & + \gamma_5 P^5 + \gamma_6 P^6 + \gamma_7 P^7) + \delta_1 \frac{A^2}{P^2} + \delta_2 \frac{A^3}{P^3} + \delta_3 \frac{A^4}{P^4}.
 \end{aligned} \tag{8}$$

#### 8.4. Effect of the Probability Function on the Star Formation Rate

The effect of applying the probability functions on the LPV stars is illustrated in Figure 10 for Field 1 and Field 2. Table 4 describes all parameters used to derive SFHs and will be available electronically. Furthermore, Tables 5 and 6 represent the star formation epochs and the total mass formed for Field 1 and Field 2, respectively. The SFHs are very similar to those

obtained without applying the corrections, but the SFRs are increased.

Having applied the probability function to each star, we derived a recent SFR of  $2.56 \times 10^{-3} M_\odot \text{ yr}^{-1} \text{ kpc}^{-2}$  and  $10^{-3} M_\odot \text{ yr}^{-1} \text{ kpc}^{-2}$  for metallicities  $Z = 0.003$  (closest match for which there are models) and  $Z = 0.008$ , respectively. These results are in the range of what Rejkuba et al. (2004a) derived for various slopes of a Salpeter IMF, viz, from  $\sim 9 \times 10^{-5}$  to  $\sim 10^{-3} M_\odot \text{ yr}^{-1} \text{ kpc}^{-2}$  (in an area of 45  $\text{kpc}^2$ ).

The SFHs we reconstruct depend on the adopted metallicity (Figures 24 and 25 in Appendix A.3). At high metallicity,  $Z = 0.010$ – $0.039$ , the SFH generally exhibits a first epoch of star formation around  $\log t(\text{yr}) \sim 10$ , followed by peaks in star formation around  $\log t(\text{yr}) \sim 9.5$  and  $\log t(\text{yr}) \sim 8.9$ . At lower metallicities, the first peak vanishes, but the other two epochs of star formation persist—if at somewhat shifted ages.

#### 8.5. Mass of the Formed Stars

From the SFH shown in Figure 10, we can determine the total stellar mass produced (Figure 11). Most stars in the two fields we study were formed up to 400 Myr ago when 93% and 96% of the stars were formed, respectively for  $Z = 0.003$  and  $Z = 0.008$ , in Field 1 (80% and 91% in Field 2). This is very similar to what Rejkuba et al. (2011) derived for a region close to Field 2, viz,  $\sim 80\%$  for these metallicities. We note that the old stellar populations have metallicities ranging from  $Z = 0.0003$  to 0.04, while the younger stars have metallicities ranging from  $Z \sim 0.002$  to 0.004 (Rejkuba et al. 2011).

We derived  $(2.83 \pm 0.61) \times 10^9 M_\odot$  and  $(2.86 \pm 0.61) \times 10^9 M_\odot$  for  $Z = 0.008$  for Field 1 and Field 2, respectively. Our derived values for Field 2 are higher than the  $4 \times 10^7 M_\odot$  reported by Rejkuba et al. (2011) for a region close to Field 2. They used the observed metallicity distribution function (MDF) for a single-age population, and then compared the observed luminosity function with the theoretical one produced by the BaSTI stellar evolutionary tracks. Their results are based on a double-burst-fitting model. We, instead, integrate the entire SFH.



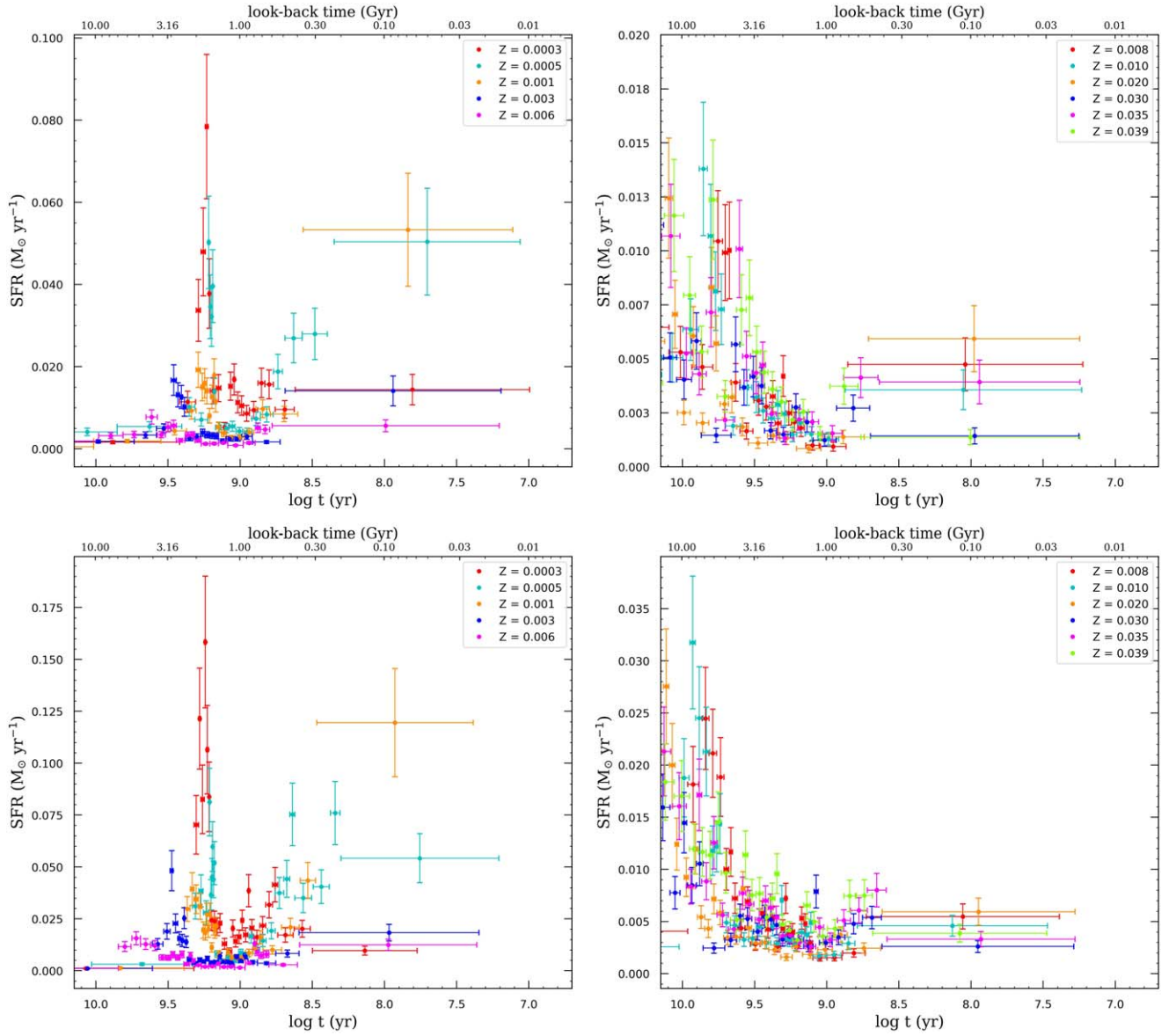


**Figure 10.** Obtained SFHs for Field 1 (upper panels) and Field 2 (lower panels) where each color represents a metallicity. The probability function was applied to the data, thus, it is seen that the SFR is raised. Each metallicity is scaled to one and the yellow regions are the desired epochs of SFR.

### 8.6. Age–Metallicity Relation

As a galaxy ages, the metallicity of the ISM—and consequently that of the new generations of stars—undergoes changes due to nucleosynthesis and feedback from dying stars. Therefore, we anticipate that older stars were formed in environments with lower metallicity compared to the environments of younger stars. Until now, we have computed the SFH assuming a constant metallicity and have not accounted for the chemical evolution of the galaxy. In this section, we will incorporate the AMRs estimated for NGC 5128 to apply this temporal variation in metallicity to the presented SFH of the galaxy.

AMRs have been derived using GCs in the NGC 5128 halo, as demonstrated in Woodley et al. (2010) and Yi et al. (2004). The appropriate metallicities for various age bins, obtained from Woodley et al. (2010), are listed in Table 7. In addition, Yi et al. (2004) presented a metallicity range of  $-2.0 \leq [\text{Fe}/\text{H}] \leq +0.3$ , which aligns with our considerations for this

galaxy. Referring to Table 2 in Yi et al. (2004), we adopt the AMR as summarized in Table 8. Utilizing these metallicity relationships, based on the suitable metallicity for different age bins, the appropriate Padova models are selected, and the mass–luminosity and age–luminosity relations are derived, as can be seen in Figure 12. Instead of employing mass–luminosity and age–luminosity relations for a constant metallicity, these new relationships, which have considered the metallicity changes of the galaxy over time, have been applied to derive the SFH, as depicted in Figure 13. In Field 1, the SFRs exhibited significant increases around  $t \sim 3.8$  Gyr and  $t \sim 800$  Myr. Meanwhile, in Field 2, we observe three epochs of star formation. The first two peaked around  $t \sim 6.3$  Gyr ago and  $t \sim 3.8$  Gyr ago, respectively. The third epoch began around  $t \sim 800$  Myr ago and peaked around  $t \sim 700$  Myr ago. The total mass produced in Field 1 using the models of Yi et al. (2004) and Woodley et al. (2010) is  $(1.03 \pm 0.12) \times 10^8 M_{\odot}$  and  $(1.04 \pm 0.12) \times 10^8 M_{\odot}$ , respectively. For Field 2, these

**Table 4**

Description of the Catalog Containing all the Parameters Needed to Derive the Star Formation Histories (Figure 10)

Column No.	Descriptor
0	Z
1	ID
2	$x$ position
3	$y$ position
4	$J$ -band magnitude
5	$H$ -band magnitude
6	$K$ -band mean magnitude
7	Probability
8	$\log$ mass ( $M_{\odot}$ )
9	$\log t$ (yr)
10	$\log \delta t$ (yr)

**Note.** Shown are the star ID,  $x$  and  $y$  positions with respect to the reference epoch (Rejkuba et al. 2003a), single-epoch  $J$ -band and  $H$ -band magnitudes, mean  $K$ -band magnitude from the sine curve fit, probability of the detection value, mass of the stars derived from the mass–luminosity relation, age of the stars derived from the age–mass relation, and LPV phase duration derived from the LPV phase duration ( $\delta t$ )–mass relation.

(This table is available in its entirety in machine-readable form in the [online article](#).)

**Table 5**

The Detected Epochs of Star Formation for Each Metallicity in Field 1

Z	Epoch 1	Epoch 2	Epoch 3	Mass ( $\times 10^8 M_{\odot}$ )
0.0003	9.23	9.04	8.85	6.20
0.0005	9.22	8.48	...	1.08
0.001	9.29	9.18	8.84	0.68
0.003	9.46	9.23	8.95	1.07
0.006	9.61	9.46	8.88	2.12
0.008	9.75	9.30	...	28.32
0.010	9.85	9.55	...	9.44
0.020	10.09	9.80	9.37	1.78
0.030	10.20	9.63	8.82	38.86
0.035	10.08	9.60	8.76	4.93
0.039	10.06	9.79	8.88	4.12

values are  $(1.60 \pm 0.23) \times 10^8 M_{\odot}$  and  $(1.50 \pm 0.23) \times 10^8 M_{\odot}$ , respectively. These estimates are only a few times higher than the value of  $4 \times 10^7 M_{\odot}$  obtained by Rejkuba et al. (2011) for a region close to Field 2.

To further understand the correlation between different populations and distinct epochs of SFHs, we have partitioned the LPV stars into four distinct period bins: 50–200, 200–400, 400–500, and 500–1100 days for Field 1 and 80–250, 250–400, 400–500, and 500–1300 days for Field 2. Utilizing the AMR models, we have constructed SFH diagrams for each of these period bins, which are depicted in Figures 14 and 15 for Field 1 and Field 2, respectively.

It is evident that the oldest epoch of star formation, occurring at  $\log t(\text{yr}) > 9.5$  ( $t$  is the lookback time), predominantly involves stars with periods ranging from 50 to 400 days in both Field 1 and Field 2. By closely examining the period–mass diagram presented in Figure 16, we can deduce that the majority of stars within the  $50 < \text{period (days)} < 400$  range are not significantly massive, possessing masses spanning from 0.2 to  $1.8 M_{\odot}$ . Notably, LPV stars with periods exceeding 400 days primarily trace intermediate and recent star formation activity.

**Table 6**

The Detected Epochs of Star Formation for Each Metallicity in Field 2

Z	Epoch 1	Epoch 2	Epoch 3	Mass ( $\times 10^8 M_{\odot}$ )
0.0003	9.24	8.94	8.76	1.41
0.0005	9.21	8.64	8.34	0.84
0.001	9.33	8.86	8.53	0.94
0.003	9.47	9.14	8.67	0.78
0.006	9.72	9.47	8.90	1.14
0.008	9.84	9.28	9.17	28.60
0.010	9.93	9.31	9.11	2.39
0.020	10.11	9.58	8.91	2.24
0.030	10.25	9.60	9.07	28.50
0.035	10.13	9.58	8.65	8.80
0.039	10.12	9.75	8.74	8.16

It is important to mention that certain studies propose deviations from the period–luminosity relation for longer periods ( $P > 400$  days). In particular, low-mass stars may experience reduced mass due to sustained heavy mass loss (Wood 2000). Conversely, the most massive AGB stars could exhibit heightened luminosity owing to the effects of hot bottom burning (Whitelock et al. 2003). Furthermore, even more massive RSGs might not adhere to a similar period–luminosity relation as AGB stars; Yang & Jiang (2012) suggest that RSGs could pulsate in the first overtone. As a result, it is important to recognize that not all stars may conform exactly to the expected behavior based solely on their periods. Hence, identifying the populations responsible for the epoch of star formation that occurred around  $\sim 800$  Myr ago is not straightforward. This is evident from Figures 14 and 15, which illustrate that both of the last period bins somewhat trace this epoch.

## 9. Discussion

### 9.1. Merger Tracers

In addition to gas accreted from the cosmic web (e.g., Dekel & Birnboim 2006; Dekel et al. 2009; Sánchez Almeida et al. 2014), mergers play critical roles in the growth of galaxies (e.g., Guo et al. 2011). Based on their progenitors’ mass ratio ( $\frac{M_1}{M_2}$ ,  $M_1 \geq M_2$ ), galaxy mergers are classified into two main categories. Major mergers (usually  $\frac{M_1}{M_2} < 4$ ) are violent and the remnant can be very different from its progenitors. Minor mergers ( $\frac{M_1}{M_2} > 4$ ) are not powerful enough to disrupt the host galaxy in each interaction. However, since giant galaxies have a significant number of satellites, minor mergers are expected to be more common and highly affect the formation and evolution of the host galaxy on cosmic timescales (Bournaud 2011). The gas content of progenitors is also another key factor in these processes. Wet mergers (in contrast to dry mergers)—mergers among gas-rich progenitors—are expected to be responsible for enhanced star formation and/or AGN activity (Mo et al. 2010). According to numerical simulations, the remnant can be determined using parameters such as the mass ratio, morphology, orbital properties, and gas content of the progenitors (Barnes 1992; Hernquist 1993; Barnes & Hernquist 1996; Dubinski et al. 1996; Springel & White 1999; Naab & Burkert 2003; Boylan-Kolchin et al. 2005; Cox et al. 2006).

The peculiar appearance of NGC 5128, especially in the form of the central disk of dust and gas (Graham 1979), optical

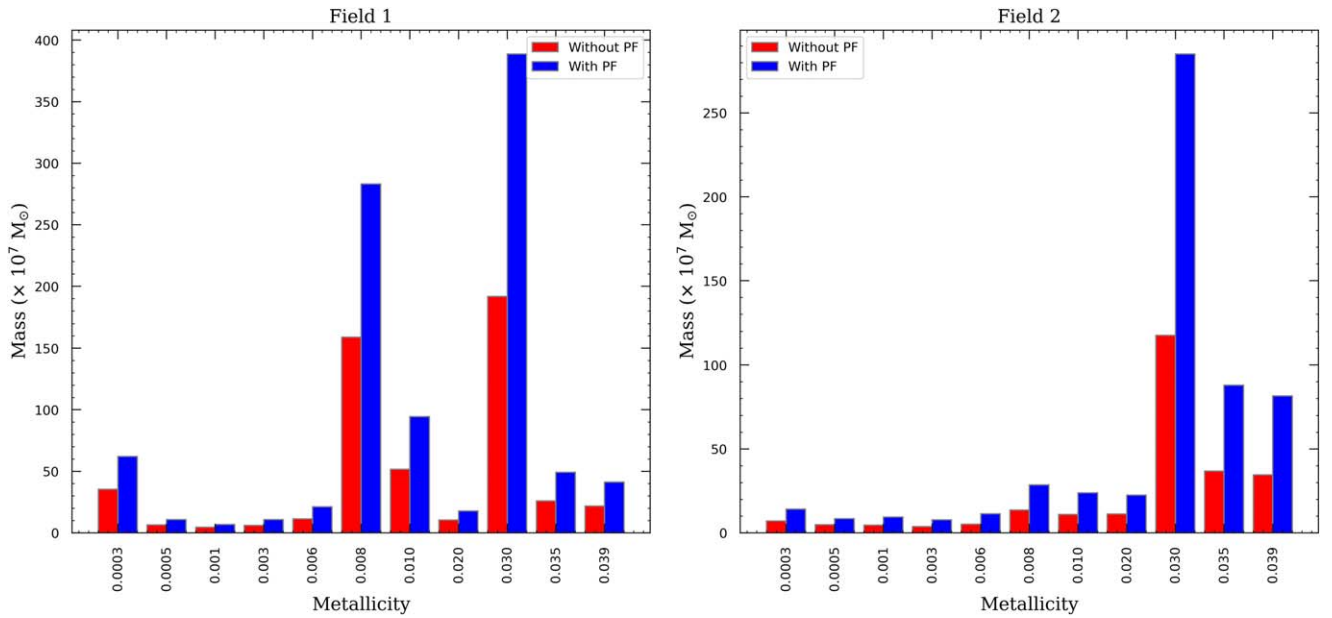


**Figure 11.** Total stellar mass derived from the SFH of Field 1 and Field 2 without and with applying a probability function.

**Table 7**

The Age–Metallicity Relation Investigated by Woodley et al. (2010) Assuming  $Z_{\odot} = 0.0198$  (Rejkuba et al. 2011)

Age Range (Gyr)	Z
age $\geq 12$	0.001
$8 \leq \text{age} < 12$	0.003
$6.5 \leq \text{age} < 8$	0.006
$5.5 \leq \text{age} < 6.5$	0.008
$3 \leq \text{age} < 5.5$	0.010
$2 \leq \text{age} < 3$	0.020
age $< 2$	0.030

**Table 8**

The Age–Metallicity Relation Investigated by Yi et al. (2004) Assuming  $Z_{\odot} = 0.0198$  (Rejkuba et al. 2011)

Age Range (Gyr)	Z
age $\geq 10$	0.0003
$6 \leq \text{age} < 10$	0.001
$4 \leq \text{age} < 6$	0.003
$3 \leq \text{age} < 4$	0.010
$2 \leq \text{age} < 3$	0.020
age $< 2$	0.039

shells (Malin et al. 1983; see also Figure 2 of Peng et al. 2002), neutral hydrogen shells (Schiminovich et al. 1994), and recent star formation (Blanco et al. 1975; Graham & Price 1981; Fassett & Graham 2000; Mould et al. 2000; Rejkuba et al. 2001) suggest that the stream of young stars was formed based as a consequence of the merging of the GE galaxy with a small gas-rich galaxy (see Israel 1998 and references therein).

Based on our results, a significant increase in star formation in Field 1 and Field 2 around 800 Myr ago (Figure 10) supports the idea of a recent merger. There are numerous works that have suggested the likely time of merger, which agree with our findings of amplified star formation. Malin et al. (1983)

interpreted the optical shell system as the aftermath of a merger with a small late-type spiral galaxy (like M33) about 1 Gyr ago. Sparke (1996) found that three-quarters of a gigayear had elapsed since the formation of the disk from the captured galaxy. Furthermore, Tubbs (1980) and Malin et al. (1983) suggested a timescale of  $2\text{--}8 \times 10^8$  yr (Israel 1998), which is supported also by Sparke (1996). Israel (1998) also proposed that the appearance of the galaxy and outcome of various dynamical models are strong indicators of at least one major merger between  $10^8$  and  $10^9$  yr ago. All of these estimates are also in full agreement with the study of GCs by Kaviraj et al. (2005) where they suggested that a starburst within  $<1$  Gyr is responsible for  $\sim 5\%$  of the stellar mass of the GCs in NGC 5128. The stellar mass of  $\sim 3\%$  we found to have formed in the last gigayear fits perfectly with their results.

Within the Centaurus group is a large number of dwarf irregular galaxies that are gas rich and host young stellar populations. As a result of dynamical friction, they transfer kinetic energy and momentum into the environment. This causes them to slow down and fall toward the host galaxy on a spiral path. As the density of the environment (halo of the host galaxy) increases, the dynamical friction grows, and infalling galaxies encounter stronger resistance from the environment. Tidal forces disrupt the infalling irregular dwarfs, resulting in a stream of stars—including young stars—in the halo of the host galaxy (Tubbs 1980; Israel 1998; Peng et al. 2002).

In addition, it appears that recent star formation in both fields, and specifically in Field 1, may be due to a minor merger  $\sim 400$  Myr ago according to Peng et al. (2002). The lower rate of star formation and lack of morphological and kinematic distortions imply this was a lesser merger than the one that had occurred  $\sim 800$  Myr ago (Wang et al. 2020).

We see another peak in star formation, between  $\log t(\text{yr}) \sim 9.4$  and  $9.6$ , in both fields, which might also have resulted from mergers or galaxy–galaxy interactions (Figure 13). There is another peak in Field 2 which is between  $\log t(\text{yr}) \sim 9.7$  and  $9.8$ . Many works confirm the existence of distinct generations of stars with similar ages,  $t \sim 3$  and  $8$  Gyr (Kaviraj et al. 2005; Rejkuba et al. 2005; Woodley et al. 2010;



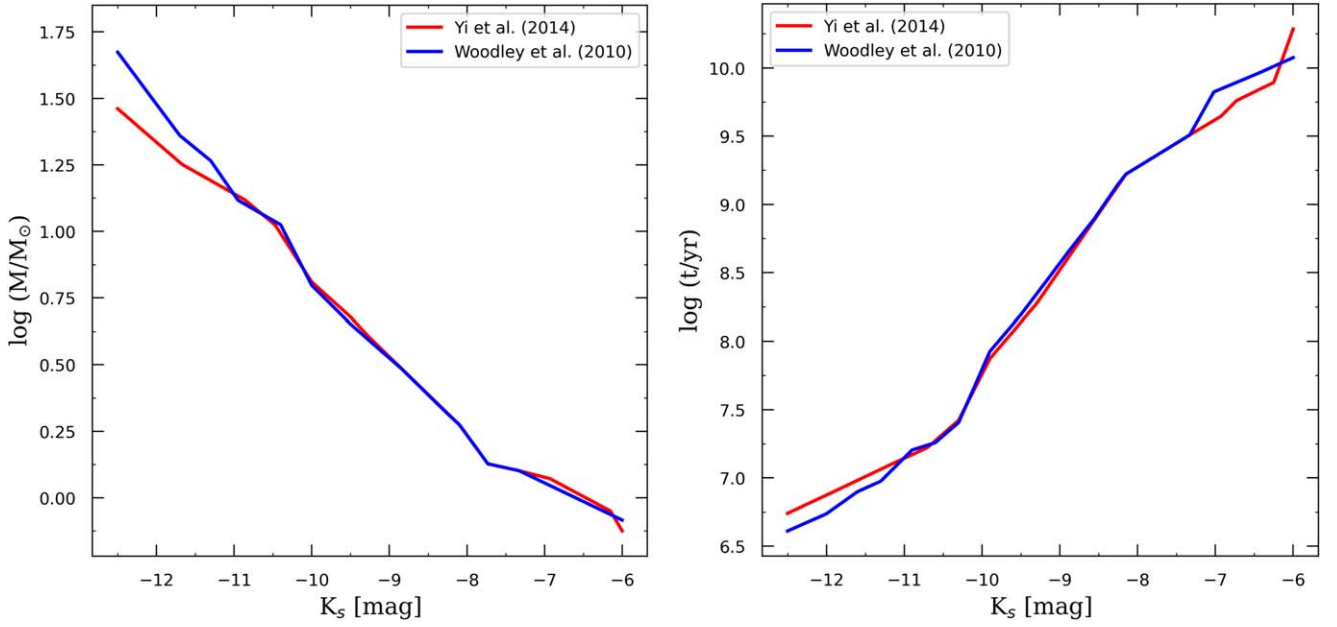


**Figure 12.** The mass–luminosity (left panel) and age–luminosity (right panel) relations by considering the AMRs of Yi et al. (2004, red line) and Woodley et al. (2010, blue line) for Field 1 (left panel) and Field 2 (right panel).

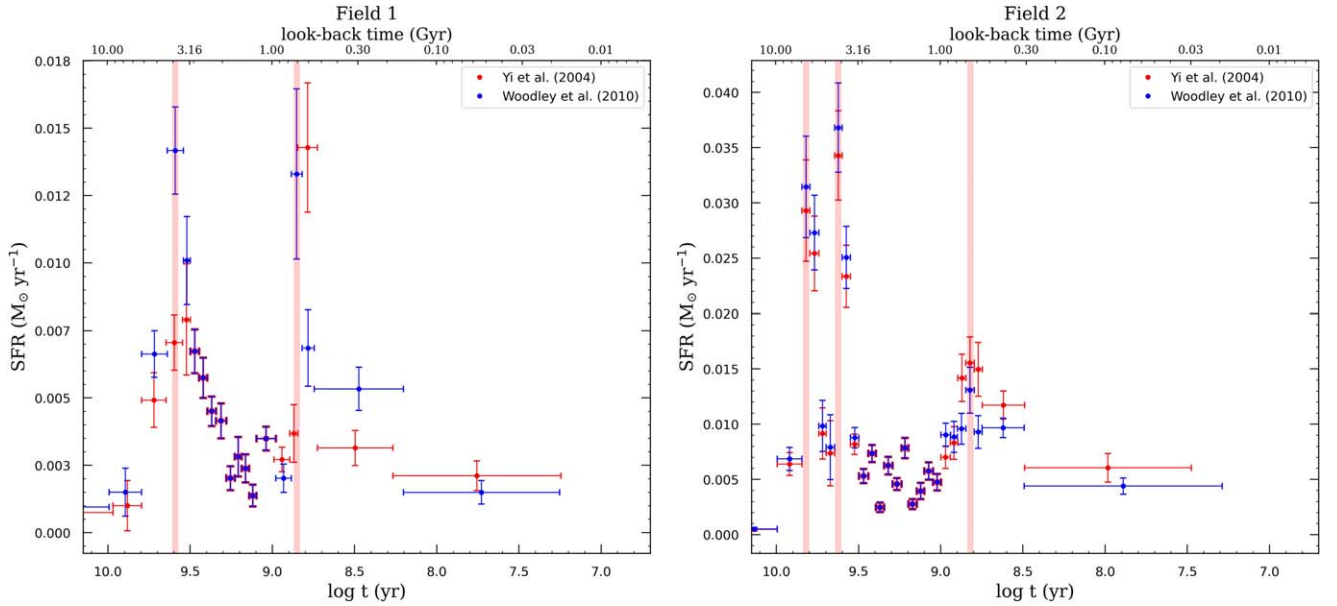


**Figure 13.** SFH derived by considering the AMRs of Yi et al. (2004, red line) and Woodley et al. (2010, blue line) for Field 1 (left panel) and Field 2 (right panel). The highlighted regions represent the peaks of star formation during the major epochs.

Rejkuba et al. 2011). Higher rates of star formation in Field 2 can be interpreted as a result of more dynamical friction effects in this field closer to the center of NGC 5128.

By comparing simulated CMDs of a remote halo field located 38 kpc south from the center of NGC 5128 (Rejkuba et al. 2005) and the CMDs obtained from HST observations, Rejkuba et al. (2011) found that the closest matches to the data are models with two bursts of star formation and an MDF. They also suggest that 80% of formed stars are old ( $\sim 12$  Gyr), while 20% of them are younger ( $\sim 2$ –3 Gyr) with lower metallicity. Rejkuba et al. (2011) also considered models with a combination of three bursts and found that in this case, using the data studied by Woodley et al. (2010), the fractions of old (11–13 Gyr), intermediate-age (6–9 Gyr), and young (3–5 Gyr)

components in the halo range between 60%–80%, 5%–15%, and 10%–20%, respectively. We obtained for Field 2 that 75% of the stars were formed 8–13 Gyr ago (for  $Z = 0.008$ ), 18% 5–8 Gyr ago, and 4% 2–5 Gyr ago. This is consistent with their two-burst scenario but also their three-burst scenario. It shows that most of the stars in the halo of NGC 5128 were formed before 400 Myr ago.

## 9.2. Active Galactic Nucleus Activity

Besides major and minor mergers, NGC 5128 has experienced AGN activity, given its central supermassive black hole (SMBH) and ample amounts of cold gas to fuel the AGN (Mo et al. 2010). In most cases, gas within galaxies is either too hot

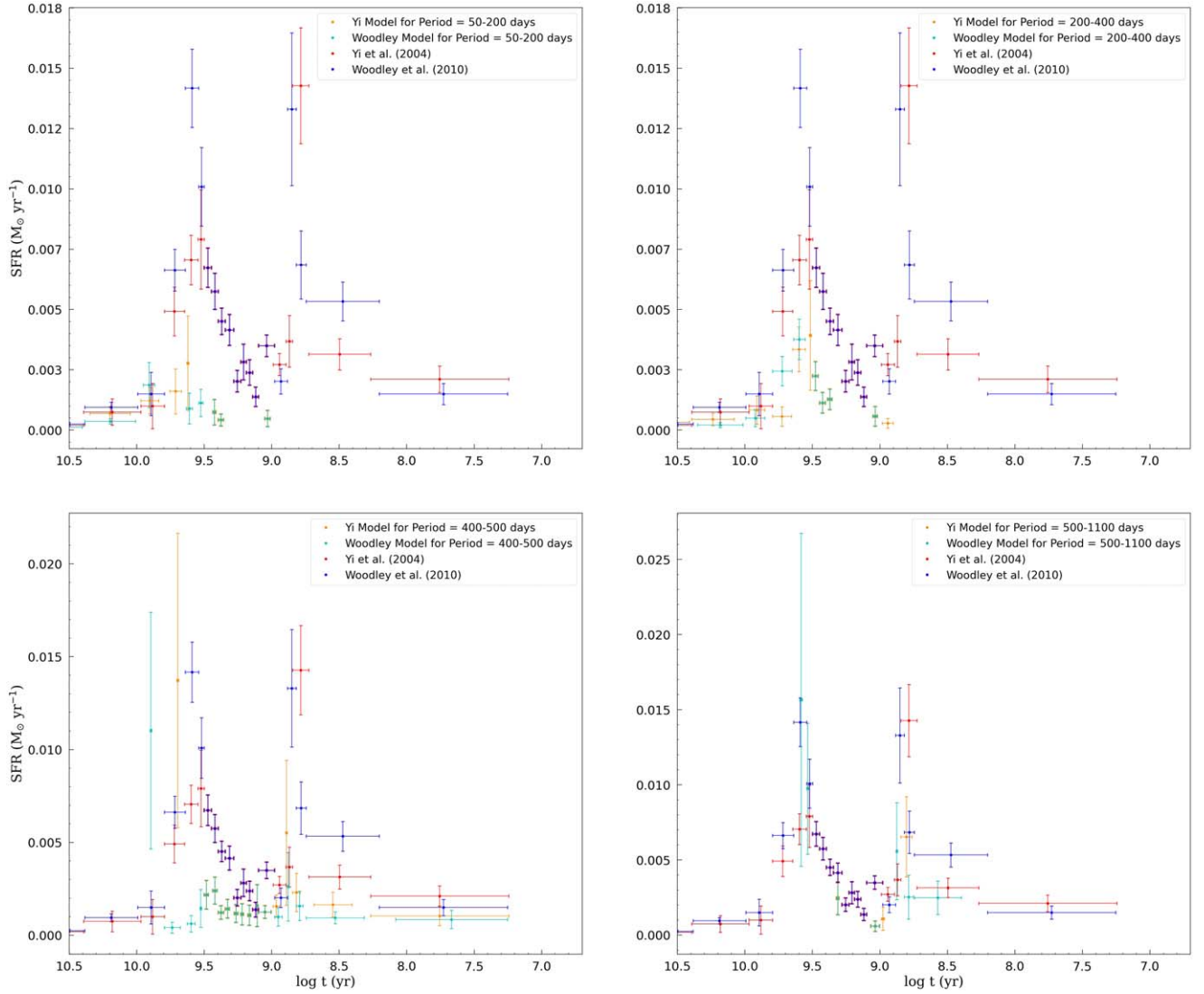


**Figure 14.** SFHs in Field 1 for four different period bins using the AMRs from Yi et al. (2004) and Woodley et al. (2010):  $P = 50\text{--}200$  days (top left),  $P = 200\text{--}400$  days (top right),  $P = 400\text{--}500$  days (bottom left), and  $P = 500\text{--}1100$  days (bottom right).

or has too much angular momentum to accrete onto the SMBH. Mergers and interactions among gas-rich galaxies (minor and major) offer ways to channel gas into the direction of the SMBH (Mo et al. 2010).

The radio jet morphology of NGC 5128 is one of the most spectacular and complicated astrophysical jets known. A pair of inner lobes—a northern inner lobe (NIL) at a distance of  $\sim 5$  kpc, and a southern inner lobe (SIL)  $\sim 11$  kpc from the center (Neff et al. 2015)—is symmetric around the AGN and oriented at an angle of  $55^\circ$  (anticlockwise) from the north-south axis (Schreier et al. 1981; Clarke et al. 1992). Further out, the NIL is followed by the NML (Morganti et al. 1999). In Figure 1, the radio emission contours from the inner lobes, as well as the NML are shown (see also Figure 1 in Morganti 2010). The NML lobe is located  $\sim 30$  kpc from the center at a position angle of  $45^\circ$  and does not show a southern counterpart in total intensity maps (Feain et al. 2011). Finally, at the largest scale, northern and southern outer lobes are seen with a total extent of  $\sim 500$  kpc end to end. The position angles of the outer lobes are lower than those of the middle and inner ones and also decrease gradually when their distances increase from the center (McKinley et al. 2013).

Here we suggest that some of the observed epochs of enhanced star formation may have been triggered by the jets. As positive AGN feedback, jet-driven shocks can cool the gas efficiently and trigger the formation of stars (Best & Heckman 2012; Ivison et al. 2012; Salomé et al. 2016b; Santoro et al. 2016; Wang et al. 2020; Joseph et al. 2022). Such positive feedback has been confirmed by observations (e.g., Emonts et al. 2014) and simulations (e.g., Fragile et al. 2004; Gaibler et al. 2012). Accepting this scenario gives us the approximate times of AGN activity or the age of the jets.

Saxton et al. (2001) estimated an age of the NML of  $\log t(\text{yr}) \sim 8.2$  ( $\sim 150$  Myr), while Hardcastle et al. (2009) determined the age of the NIL and SIL to be  $\log t(\text{yr}) \sim 7.5$  ( $\sim 30$  Myr). Also, they found that a jet passed through the NIL and intruded into the NML, indicating that activity has continued and enriched the NML. Therefore, recent AGN activity should be considered as a potential factor in recent star formation in the halo of NGC 5128 (Hardcastle et al. 2009), in agreement with the SFRs from  $\log t(\text{yr}) \sim 7.2$  to  $8.2$  for the NIL/SIL and NML lobes. We thus propose that the enhanced star formation around 800 Myr ago might be associated with

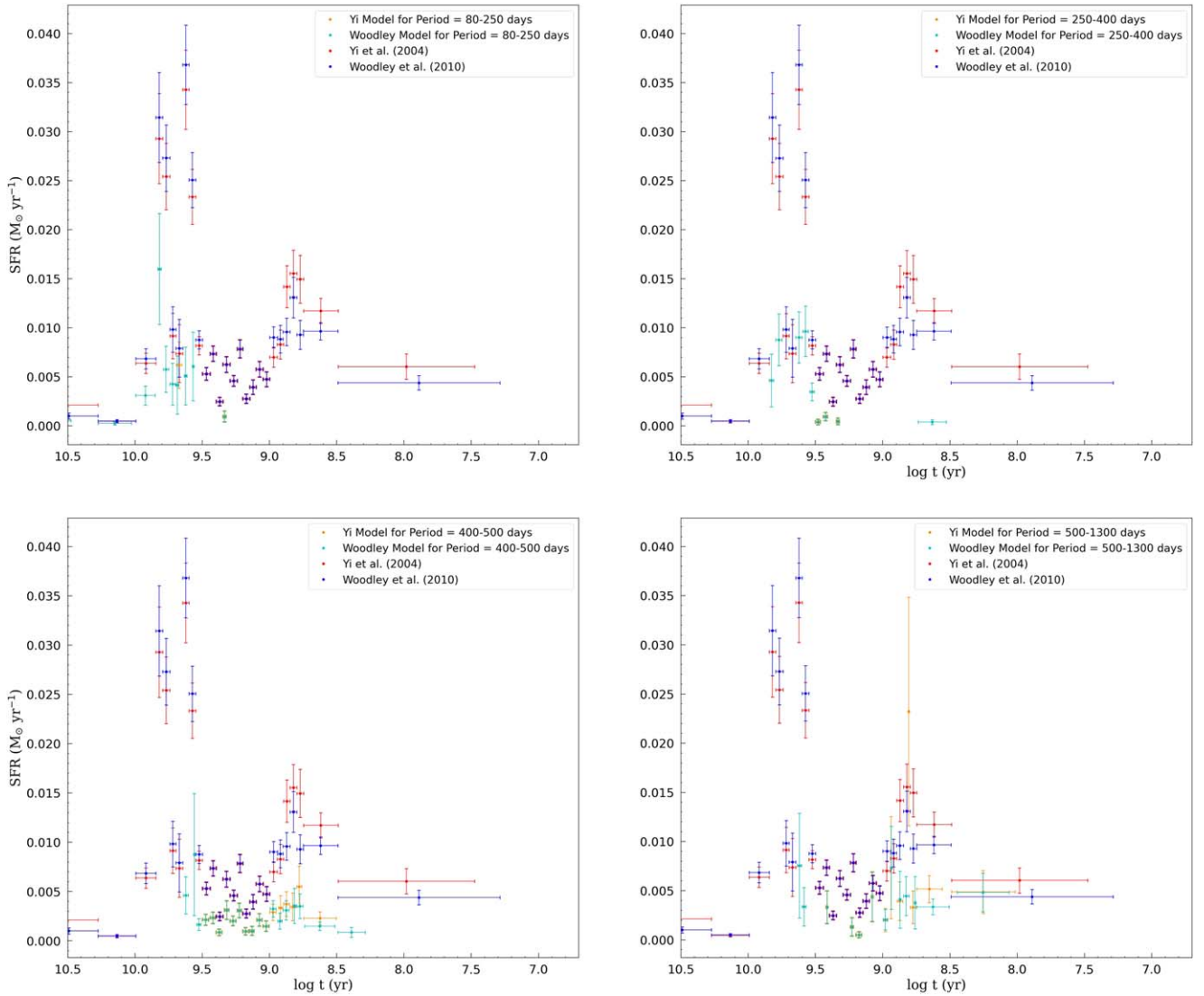


**Figure 15.** SFHs in Field 2 for four different period bins using the AMRs from Yi et al. (2004) and Woodley et al. (2010):  $P = 80\text{--}250$  days (top left),  $P = 250\text{--}400$  days (top right),  $P = 400\text{--}500$  days (bottom left), and  $P = 500\text{--}1300$  days (bottom right).

the outer lobes, which resulted from enhanced AGN activity due to a wet minor merger around that time.

### 9.3. NGC 5128 Evolution

Deriving the SFH in the host galaxy resulting from a merger is complicated. As we explained in Section 6, the SFRs we derive are based on identified LPV stars. These may have formed in NGC 5128 (in situ) or outside of it (ex situ, in a merging galaxy). Therefore, both in situ and ex situ stars can amplify the apparent SFR in the halo of NGC 5128. The time of amplification by in situ or ex situ stars that are formed during the merger process (for a review of star formation during mergers and interactions, see Bournaud 2011) is equal to the time interval over which the host galaxy captures the infalling galaxy. Amplification by ex situ stars can, however, occur also in another, independent way, namely within the infalling galaxy before it started merging. In this case, it occurs much earlier than the accretion event, and reflects the evolution of the infalling galaxy, not NGC 5128 or the merger.

The stars of a small galaxy falling into a more massive halo will form shells (Quinn 1984; Dupraz & Combes 1987). The

dynamics of the gas from such merging galaxy is however not well understood. Based on some simple simulations, Weil & Hernquist (1993) concluded that dissipation would result in rapid concentration in the center. On the other hand, the detection of  $4 \times 10^8 M_\odot$  of H I gas associated with the stellar shells (with a small displacement) by Schiminovich et al. (1994) contradicts their claim. Combes & Charmandaris (1999) and Charmandaris et al. (2000) suggested that if the ISM of the merging galaxy is clumpy then the collision and dissipation rates are low. There is clear evidence of star formation going on in the halo, but it only happens along the jet (e.g., Rejkuba et al. 2001; Joseph et al. 2022), and it is relatively inefficient (Salomé et al. 2016b, 2017). Therefore, it seems that any elevated levels of star formation that occur during the merger process will likely happen within the secondary galaxy in addition to the halo of the host galaxy.

As illustrated in Schiminovich et al. (1994), there are three main H I clouds in NGC 5128, two of which are in similar positions to Field 1 and Field 2. They found that star formation continues at the location of Field 1. Oosterloo & Morganti (2004) and Mould et al. (2000) reported recent SFR in the H I cloud near Field 1 of a few times  $10^{-3} M_\odot \text{ yr}^{-1}$ , while



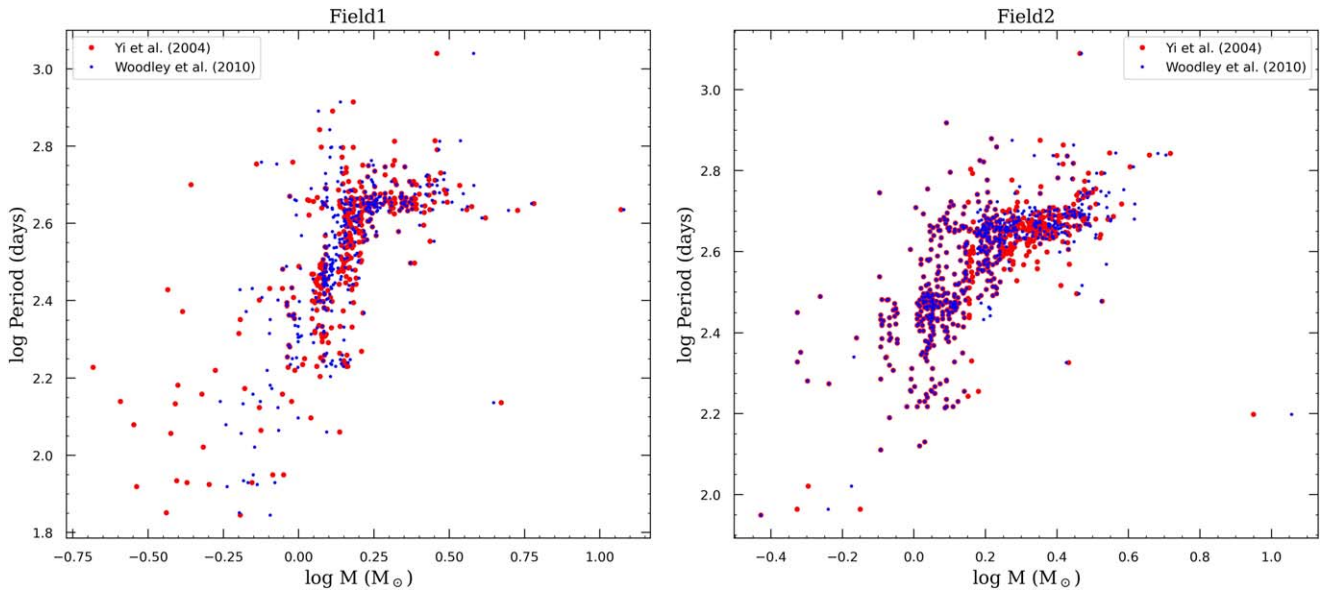


**Figure 16.** Pulsation period of LPV stars vs. mass for Field 1 (left panel) and Field 2 (right panel). The blue and red dots refer to the AMR models of Woodley et al. (2010) and Yi et al. (2004), respectively.

Salomé et al. (2016b) obtained  $4 \times 10^{-3} M_{\odot} \text{ yr}^{-1}$  (at low metallicity); this is similar to what we derived for metallicities in the range  $0.008 < Z < 0.039$ . Field 2 has not been studied as much as Field 1, but given our results agree with those obtained for Field 1, this lends some credibility for our results in Field 2. Santoro et al. (2015a, 2015b) and Santoro et al. (2016) suggested that ionization by young stars ( $< 4$  Myr) and AGN shocks traces the interaction between the AGN jet and gas from an accreted galaxy.

We identified two epochs of increased star formation for Field 1 around  $\log t(\text{yr}) \sim 8.9$  and  $9.6$ , and for Field 2 at  $\log t(\text{yr}) \sim 8.9$ ,  $9.6$ , and  $9.8$  (Figure 13). The latest epoch of enhanced star formation at  $\log t(\text{yr}) \sim 8.9$  can be linked with a minor wet merger, where star formation took place primarily within the merging galaxy rather than in the halo of NGC 5128—timescales of  $< 1$  Gyr are in agreement with such a scenario (Israel 1998). There is no such evidence for previous mergers that could be responsible for the more ancient epochs of elevated SFRs around  $\log t(\text{yr}) \sim 9.6$  and  $9.8$ . While we cannot rule out past mergers, it is also conceivable that those older stars actually had formed in the galaxy before it merged with NGC 5128 around  $\log t(\text{yr}) \sim 8.9$  (Israel 1998). This would make it a relatively massive merger.

Peng et al. (2002) referred to the large number of dwarf irregular galaxies in the Centaurus group, rendering it plausible that a gas-rich merger and the supply of an already formed relatively youthful stellar population enriched the halo of NGC 5128. Rejkuba et al. (2022), too, argued that the extended, 2–3 Gyr old stellar population points at the accretion of a small gas-rich spiral galaxy having provided the fuel for ongoing star formation at the center of NGC 5128. The recent merger,  $< 2 \times 10^8$  yr ago, requires that the intermediate-age stars came from either that accreted galaxy or a previous merger (Rejkuba et al. 2022).

Our analysis is based on fields located far from the center. Gas and stars have different dynamics during mergers or interactions within the halo; gas cannot form stars efficiently and eventually ends up in the center (Rejkuba et al. 2002; Israel 1998). A complementary study of the central part of the

galaxy could provide more certainty about the history of the halo. Unfortunately, to date, there is no LPV catalog of the inner parts of the galaxy. Conducting a survey for LPV stars in the outer part of the central disk (where it is less crowded and obscured) could be a promising approach.

Finally, we note that thus far the application of our LPV method was limited to galaxies within the LG. Now, for the first time, we have used it to find the SFH of a galaxy outside the LG. Our results strongly confirm the reliability of the method even for such distant galaxies and using ground-based observations.

## 10. Summary of Conclusions

NGC 5128 is the nearest GE galaxy at a distance of 3.8 Mpc. Based on its resolved stellar populations and prominent features such as AGN activity, this galaxy has been extensively studied. It is expected to become a popular target for future large telescopes. In this paper, we have used a novel method to find the SFHs of two fields in the halo of the NGC 5128 galaxy—Field 1 is in the northeastern, which is  $\sim 17'$  ( $\sim 18.8$  kpc) away from the center of the galaxy, and Field 2 is located in the southern part at a distance of  $\sim 9'$  ( $\sim 9.9$  kpc) from the center. Our method is based on the identification of 395 LPV stars in Field 1 and 671 LPV stars in Field 2. Our main results are as follows.

1. Even though the two fields are located 28 kpc away from each other on different sides of the galaxy, they show similar SFHs. In Field 1, the SFR increased significantly around  $t \sim 800$  Myr and  $t \sim 3.8$  Gyr; in Field 2, the SFR increased considerably around  $t \sim 800$  Myr,  $t \sim 3.8$  Gyr, and  $t \sim 6.3$  Gyr, where  $t$  is the lookback time.
2. To account for incompleteness, we constructed a probability function with dependency on amplitude, period, and magnitude. Applying this correction by giving a weight to each identified LPV results in a more accurate SFR.

3. We postulate that the enhanced SFR around  $t \sim 800$  Myr ago may have been the result of triggered star formation by a merger that happened  $t \sim 1$  Gyr ago.

### Acknowledgments

We thank the referee for the useful report which prompted us to improve the manuscript.

### Appendix Supplementary Material

#### A.1. Padova Evolutionary Model

In order to find the SFH based on the LPV star counts, we need to determine the mass, age, and LPV phase duration of each LPV star (Javadi et al. 2011b, 2011c, 2017; Rezaei et al. 2014; Hamedani Golshan et al. 2017; Hashemi et al. 2019; Navabi et al. 2021; Saremi et al. 2021). First we assume the metallicity, then we link observational fluxes (for  $Ks$ -band

magnitude) of each star to its mass, and finally, we estimate the age and LPV phase duration from the derived mass. In this paper, we have assumed 11 different metallicities (covering the whole range of metallicities in the fields of study) to extract the associated Padova evolutionary models (see Section 4) and obtain equations for describing the fitted curves and lines. Preferably, we use the final version of the Padova model (Marigo et al. 2017), but given that the final version does not consider the variability of massive stars, we use the previous release (Marigo et al. 2008) only for the LPV phase duration of massive stars ( $\log(M/M_{\odot}) > 0.8$ ).

The mass, age, and LPV phase duration relations are investigated by using the IRAF software. The related coefficients can be found in Tables 9, 10, and 11 for various ranges, and the set shown in Figure 17 depicts linear and multi-Gaussian fits to the obtained data, which are the peak of magnitude in each age of the theoretical isochrones from the Padova evolutionary models (Marigo et al. 2017).

**Table 9**

Fitting Equations of the Relation between Birth Mass and  $Ks$ -band Magnitude,  $\log M/M_{\odot} = aK + b$ , for a Distance Modulus of  $\mu = 27.87$  mag (Rejkuba et al. 2004a)

a	b	Validity Range
$Z = 0.0003$		
$-0.107 \pm 0.181$	$0.497 \pm 2.124$	$Ks \leq -11.984$
$-0.312 \pm 0.182$	$-1.965 \pm 2.062$	$-11.984 < Ks \leq -11.534$
$-0.249 \pm 0.128$	$-131.238 \pm 1.390$	$-11.534 < Ks \leq -11.083$
$-0.520 \pm 0.098$	$-4.239 \pm 1.028$	$-11.083 < Ks \leq -10.633$
$-0.278 \pm 0.087$	$-1.669 \pm 0.863$	$-10.633 < Ks \leq -10.182$
$-0.660 \pm 0.118$	$-5.564 \pm 1.112$	$-10.182 < Ks \leq -9.732$
$-0.602 \pm 0.113$	$-4.993 \pm 1.031$	$-9.732 < Ks \leq -9.281$
$-0.181 \pm 0.083$	$-1.088 \pm 0.717$	$-9.281 < Ks \leq -8.830$
$-0.310 \pm 0.084$	$-2.226 \pm 0.687$	$-8.830 < Ks \leq -8.380$
$-0.225 \pm 0.083$	$-1.514 \pm 0.640$	$-8.380 < Ks \leq -7.929$
$-0.189 \pm 0.129$	$-1.227 \pm 0.922$	$-7.929 < Ks \leq -7.479$
$-0.074 \pm 0.137$	$-0.367 \pm 0.943$	$-7.479 < Ks \leq -7.028$
$-0.066 \pm 0.107$	$-0.310 \pm 0.676$	$-7.028 < Ks \leq -6.578$
$-0.491 \pm 0.091$	$-3.106 \pm 0.544$	$Ks > -6.578$
$Z = 0.0005$		
$-0.121 \pm 0.227$	$0.309 \pm 2.663$	$Ks \leq -12.011$
$-0.281 \pm 0.226$	$-1.614 \pm 2.558$	$-12.011 < Ks \leq -11.535$
$-0.443 \pm 0.143$	$-3.475 \pm 1.554$	$-11.535 < Ks \leq -11.060$
$-0.414 \pm 0.123$	$-3.160 \pm 1.265$	$-11.060 < Ks \leq -10.584$
$-0.231 \pm 0.126$	$-1.217 \pm 1.247$	$-10.584 < Ks \leq -10.108$
$-0.729 \pm 0.118$	$-6.259 \pm 1.103$	$-10.108 < Ks \leq -9.632$
$-0.344 \pm 0.126$	$-2.547 \pm 1.123$	$-9.632 < Ks \leq -9.156$
$-0.151 \pm 0.111$	$-0.774 \pm 0.941$	$-9.156 < Ks \leq -8.681$
$-0.354 \pm 0.093$	$-2.538 \pm 0.740$	$-8.681 < Ks \leq -8.205$
$-0.345 \pm 0.152$	$-2.463 \pm 1.123$	$-8.205 < Ks \leq -7.729$
$-0.045 \pm 0.196$	$-0.144 \pm 1.383$	$-7.729 < Ks \leq -7.253$
$-0.122 \pm 0.144$	$-0.710 \pm 0.947$	$-7.253 < Ks \leq -6.778$
$-0.231 \pm 0.140$	$-1.443 \pm 0.840$	$-6.778 < Ks \leq -6.302$
$-0.139 \pm 0.125$	$-0.866 \pm 0.706$	$Ks > -6.302$
$Z = 0.001$		
$-0.011 \pm 0.303$	$1.684 \pm 3.566$	$Ks \leq -12.033$
$-0.590 \pm 0.262$	$-5.274 \pm 2.996$	$-12.033 < Ks \leq -11.573$
$-0.375 \pm 0.176$	$-2.795 \pm 1.915$	$-11.573 < Ks \leq -11.114$
$-0.347 \pm 0.187$	$-2.484 \pm 1.948$	$-11.114 < Ks \leq -10.654$
$-0.300 \pm 0.165$	$-1.979 \pm 1.646$	$-10.654 < Ks \leq -10.195$
$-0.376 \pm 0.150$	$-2.752 \pm 1.428$	$-10.195 < Ks \leq -9.735$
$-0.561 \pm 0.155$	$-4.552 \pm 1.399$	$-9.735 < Ks \leq -9.276$

**Table 9**  
(Continued)

a	b	Validity Range
$-0.255 \pm 0.140$	$-1.714 \pm 1.204$	$-9.276 < Ks \leq -8.816$
$-0.414 \pm 0.115$	$-3.117 \pm 0.941$	$-8.816 < Ks \leq -8.357$
$-0.280 \pm 0.139$	$-1.996 \pm 1.056$	$-8.357 < Ks \leq -7.897$
$-0.082 \pm 0.203$	$-0.432 \pm 1.453$	$-7.897 < Ks \leq -7.438$
$-0.108 \pm 0.208$	$-0.626 \pm 1.409$	$-7.438 < Ks \leq -6.978$
$-0.216 \pm 0.170$	$-1.381 \pm 1.070$	$-6.978 < Ks \leq -6.518$
$-0.204 \pm 0.130$	$-1.305 \pm 0.764$	$Ks > -6.518$
<hr/>		
$Z = 0.003$		
$-0.538 \pm 0.085$	$-4.810 \pm 0.983$	$Ks \leq -11.827$
$-0.449 \pm 0.086$	$-3.763 \pm 0.967$	$-11.827 < Ks \leq -11.408$
$-0.219 \pm 0.101$	$-1.134 \pm 1.090$	$-11.408 < Ks \leq -10.990$
$-0.311 \pm 0.101$	$-2.151 \pm 1.047$	$-10.990 < Ks \leq -10.571$
$-0.211 \pm 0.093$	$-1.093 \pm 0.926$	$-10.571 < Ks \leq -10.152$
$-0.676 \pm 0.115$	$-5.818 \pm 1.088$	$-10.152 < Ks \leq -9.733$
$-0.287 \pm 0.110$	$-2.030 \pm 1.006$	$-9.733 < Ks \leq -9.315$
$-0.311 \pm 0.073$	$-2.251 \pm 0.639$	$-9.315 < Ks \leq -8.896$
$-0.401 \pm 0.067$	$-3.049 \pm 0.552$	$-8.896 < Ks \leq -8.477$
$-0.216 \pm 0.067$	$-1.481 \pm 0.525$	$-8.477 < Ks \leq -8.058$
$-0.235 \pm 0.090$	$-1.636 \pm 0.664$	$-8.058 < Ks \leq -7.639$
$-0.102 \pm 0.102$	$-0.623 \pm 0.718$	$-7.639 < Ks \leq -7.221$
$-0.173 \pm 0.085$	$-1.130 \pm 0.560$	$-7.221 < Ks \leq -6.802$
$-0.218 \pm 0.069$	$-1.436 \pm 0.431$	$Ks > -6.802$
<hr/>		
$Z = 0.006$		
$-0.459 \pm 0.136$	$-3.888 \pm 1.602$	$Ks \leq -11.902$
$-0.623 \pm 0.127$	$-5.844 \pm 1.426$	$-11.902 < Ks \leq -11.498$
$-0.159 \pm 0.156$	$-0.508 \pm 1.698$	$-11.498 < Ks \leq -11.094$
$-0.280 \pm 0.142$	$-1.851 \pm 1.493$	$-11.094 < Ks \leq -10.689$
$-0.298 \pm 0.146$	$-2.036 \pm 1.474$	$-10.689 < Ks \leq -10.285$
$-0.355 \pm 0.244$	$-2.623 \pm 2.344$	$-10.285 < Ks \leq -9.881$
$-0.529 \pm 0.230$	$-4.347 \pm 2.148$	$-9.881 < Ks \leq -9.477$
$-0.240 \pm 0.112$	$-1.605 \pm 0.999$	$-9.477 < Ks \leq -9.073$
$-0.397 \pm 0.102$	$-3.031 \pm 0.862$	$-9.073 < Ks \leq -8.669$
$-0.111 \pm 0.113$	$-0.555 \pm 0.915$	$-8.669 < Ks \leq -8.265$
$-0.405 \pm 0.110$	$-2.981 \pm 0.841$	$-8.265 < Ks \leq -7.860$
$-0.198 \pm 0.108$	$-1.355 \pm 0.785$	$-7.860 < Ks \leq -7.456$
$-0.200 \pm 0.107$	$-1.371 \pm 0.734$	$-7.456 < Ks \leq -7.052$
$-0.200 \pm 0.095$	$-1.372 \pm 0.614$	$Ks > -7.052$
<hr/>		
$Z = 0.008$		
$-0.767 \pm 0.131$	$-7.575 \pm 1.522$	$Ks \leq -11.767$
$-0.412 \pm 0.140$	$-3.402 \pm 1.563$	$-11.767 < Ks \leq -11.381$
$-0.139 \pm 0.165$	$-0.298 \pm 1.781$	$-11.381 < Ks \leq -10.994$
$-0.346 \pm 0.139$	$-2.565 \pm 1.449$	$-10.994 < Ks \leq -10.608$
$-0.195 \pm 0.126$	$-0.972 \pm 1.265$	$-10.608 < Ks \leq -10.221$
$-0.671 \pm 0.173$	$-5.838 \pm 1.661$	$-10.221 < Ks \leq -9.835$
$-0.200 \pm 0.167$	$-1.198 \pm 1.550$	$-9.835 < Ks \leq -9.448$
$-0.390 \pm 0.101$	$-2.999 \pm 0.896$	$-9.448 < Ks \leq -9.061$
$-0.368 \pm 0.089$	$-2.796 \pm 0.756$	$-9.061 < Ks \leq -8.675$
$-0.307 \pm 0.095$	$-2.269 \pm 0.770$	$-8.675 < Ks \leq -8.288$
$-0.210 \pm 0.102$	$-1.461 \pm 0.780$	$-8.288 < Ks \leq -7.902$
$-0.271 \pm 0.110$	$-1.948 \pm 0.807$	$-7.902 < Ks \leq -7.515$
$-0.161 \pm 0.107$	$-1.117 \pm 0.740$	$-7.515 < Ks \leq -7.129$
$-0.180 \pm 0.108$	$-1.258 \pm 0.705$	$Ks > -7.129$
<hr/>		
$Z = 0.010$		
$-0.750 \pm 0.139$	$-7.390 \pm 1.617$	$Ks \leq -11.777$
$-0.402 \pm 0.143$	$-3.296 \pm 1.599$	$-11.777 < Ks \leq -11.396$
$-0.173 \pm 0.165$	$-0.677 \pm 1.788$	$-11.396 < Ks \leq -11.016$
$-0.310 \pm 0.141$	$-2.189 \pm 1.479$	$-11.016 < Ks \leq -10.635$
$-0.217 \pm 0.137$	$-1.196 \pm 1.382$	$-10.635 < Ks \leq -10.254$
$-0.583 \pm 0.162$	$-4.950 \pm 1.562$	$-10.254 < Ks \leq -9.873$



**Table 9**  
(Continued)

a	b	Validity Range
$-0.305 \pm 0.150$	$-2.210 \pm 1.399$	$-9.873 < Ks \leq -9.492$
$-0.309 \pm 0.104$	$-2.245 \pm 0.929$	$-9.492 < Ks \leq -9.112$
$-0.410 \pm 0.093$	$-3.168 \pm 0.790$	$-9.112 < Ks \leq -8.731$
$-0.292 \pm 0.108$	$-2.137 \pm 0.883$	$-8.731 < Ks \leq -8.350$
$-0.249 \pm 0.105$	$-1.776 \pm 0.816$	$-8.350 < Ks \leq -7.969$
$-0.324 \pm 0.099$	$-2.376 \pm 0.735$	$-7.969 < Ks \leq -7.589$
$-0.156 \pm 0.109$	$-1.102 \pm 0.765$	$-7.589 < Ks \leq -7.208$
$-0.166 \pm 0.117$	$-1.170 \pm 0.776$	$Ks > -7.208$
<hr/>		
$Z = 0.02$		
$-0.521 \pm 0.104$	$-4.732 \pm 1.192$	$Ks \leq -11.622$
$-0.274 \pm 0.117$	$-1.866 \pm 1.295$	$-11.622 < Ks \leq -11.279$
$-0.207 \pm 0.117$	$-1.101 \pm 1.258$	$-11.279 < Ks \leq -10.936$
$-0.230 \pm 0.110$	$-1.357 \pm 1.151$	$-10.936 < Ks \leq -10.593$
$-0.203 \pm 0.107$	$-1.068 \pm 1.077$	$-10.593 < Ks \leq -10.250$
$-0.585 \pm 0.124$	$-4.991 \pm 1.207$	$-10.250 < Ks \leq -9.907$
$-0.298 \pm 0.115$	$-2.147 \pm 1.085$	$-9.907 < Ks \leq -9.564$
$-0.319 \pm 0.077$	$-2.348 \pm 0.699$	$-9.564 < Ks \leq -9.221$
$-0.344 \pm 0.067$	$-2.577 \pm 0.580$	$-9.221 < Ks \leq -8.878$
$-0.328 \pm 0.065$	$-2.429 \pm 0.548$	$-8.878 < Ks \leq -8.535$
$-0.414 \pm 0.064$	$-3.166 \pm 0.514$	$-8.535 < Ks \leq -8.192$
$-0.349 \pm 0.067$	$-2.638 \pm 0.515$	$-8.192 < Ks \leq -7.849$
$-0.217 \pm 0.080$	$-1.601 \pm 0.583$	$-7.849 < Ks \leq -7.506$
$-0.130 \pm 0.099$	$-0.958 \pm 0.696$	$Ks > -7.506$
<hr/>		
$Z = 0.030$		
$-0.391 \pm 0.166$	$-3.214 \pm 1.910$	$Ks \leq -11.618$
$-0.219 \pm 0.128$	$-1.210 \pm 1.427$	$-11.618 < Ks \leq -11.290$
$-0.413 \pm 0.140$	$-3.407 \pm 1.514$	$-11.290 < Ks \leq -10.961$
$-0.133 \pm 0.147$	$-0.338 \pm 1.535$	$-10.961 < Ks \leq -10.633$
$-0.257 \pm 0.195$	$-1.649 \pm 1.965$	$-10.633 < Ks \leq -10.305$
$-0.647 \pm 0.183$	$-5.668 \pm 1.806$	$-10.305 < Ks \leq -9.977$
$-0.284 \pm 0.104$	$-2.050 \pm 0.985$	$-9.977 < Ks \leq -9.649$
$-0.249 \pm 0.106$	$-1.713 \pm 0.970$	$-9.649 < Ks \leq -9.320$
$-0.296 \pm 0.106$	$-2.148 \pm 0.937$	$-9.320 < Ks \leq -8.992$
$-0.171 \pm 0.102$	$-1.023 \pm 0.868$	$-8.992 < Ks \leq -8.664$
$-0.307 \pm 0.100$	$-2.208 \pm 0.822$	$-8.664 < Ks \leq -8.336$
$-0.360 \pm 0.087$	$-2.646 \pm 0.682$	$-8.336 < Ks \leq -8.007$
$-0.360 \pm 0.087$	$-2.649 \pm 0.656$	$-8.007 < Ks \leq -7.679$
$-0.353 \pm 0.089$	$-2.617 \pm 0.649$	$Ks > -7.679$
<hr/>		
$Z = 0.035$		
$-0.275 \pm 0.079$	$-1.949 \pm 0.920$	$Ks \leq -11.758$
$-0.198 \pm 0.088$	$-1.040 \pm 0.991$	$-11.758 < Ks \leq -11.415$
$-0.168 \pm 0.094$	$-0.698 \pm 1.025$	$-11.415 < Ks \leq -11.073$
$-0.222 \pm 0.086$	$-1.296 \pm 0.904$	$-11.073 < Ks \leq -10.731$
$-0.146 \pm 0.081$	$-0.481 \pm 0.827$	$-10.731 < Ks \leq -10.388$
$-0.502 \pm 0.086$	$-4.179 \pm 0.847$	$-10.388 < Ks \leq -10.046$
$-0.505 \pm 0.075$	$-4.214 \pm 0.717$	$-10.046 < Ks \leq -9.704$
$-0.113 \pm 0.063$	$-0.408 \pm 0.574$	$-9.704 < Ks \leq -9.361$
$-0.361 \pm 0.059$	$-2.732 \pm 0.525$	$-9.361 < Ks \leq -9.019$
$-0.164 \pm 0.054$	$-0.951 \pm 0.462$	$-9.019 < Ks \leq -8.676$
$-0.304 \pm 0.048$	$-2.169 \pm 0.392$	$-8.676 < Ks \leq -8.334$
$-0.383 \pm 0.043$	$-2.830 \pm 0.336$	$-8.334 < Ks \leq -7.992$
$-0.342 \pm 0.045$	$-2.502 \pm 0.337$	$-7.992 < Ks \leq -7.649$
$-0.331 \pm 0.047$	$-2.418 \pm 0.333$	$Ks > -7.649$
<hr/>		
$Z = 0.039$		
$-0.254 \pm 0.025$	$-1.714 \pm 0.286$	$Ks \leq -11.783$
$-0.190 \pm 0.027$	$-0.963 \pm 0.301$	$-11.783 < Ks \leq -11.419$
$-0.159 \pm 0.028$	$-0.611 \pm 0.304$	$-11.419 < Ks \leq -11.054$
$-0.202 \pm 0.025$	$-1.077 \pm 0.264$	$-11.054 < Ks \leq -10.689$
$-0.241 \pm 0.029$	$-1.499 \pm 0.292$	$-10.689 < Ks \leq -10.325$

**Table 9**  
(Continued)

a	b	Validity Range
$-0.564 \pm 0.029$	$-4.835 \pm 0.282$	$-10.325 < Ks \leq -9.960$
$-0.200 \pm 0.020$	$-1.207 \pm 0.191$	$-9.960 < Ks \leq -9.595$
$-0.311 \pm 0.015$	$-2.276 \pm 0.140$	$-9.595 < Ks \leq -9.231$
$-0.275 \pm 0.015$	$-1.942 \pm 0.130$	$-9.231 < Ks \leq -8.866$
$-0.225 \pm 0.015$	$-1.498 \pm 0.126$	$-8.866 < Ks \leq -8.502$
$-0.343 \pm 0.014$	$-2.502 \pm 0.113$	$-8.502 < Ks \leq -8.137$
$-0.343 \pm 0.014$	$-2.501 \pm 0.107$	$-8.137 < Ks \leq -7.772$
$-0.326 \pm 0.015$	$-2.370 \pm 0.107$	$-7.772 < Ks \leq -7.408$
$-0.347 \pm 0.043$	$-2.528 \pm 0.293$	$Ks > -7.408$

**Table 10**  
Fitting Equations of the Relation between Age and Birth Mass,  $\log t = a \log M + b$ 

a	b	Validity Range
$Z = 0.0003$		
$-3.202 \pm 0.021$	$9.772 \pm 0.005$	$\log M \leq 0.128$
$-2.629 \pm 0.019$	$9.699 \pm 0.009$	$0.128 < \log M \leq 0.370$
$-2.394 \pm 0.020$	$9.612 \pm 0.015$	$0.370 < \log M \leq 0.612$
$-2.007 \pm 0.022$	$9.375 \pm 0.021$	$0.612 < \log M \leq 0.854$
$-1.681 \pm 0.024$	$9.096 \pm 0.030$	$0.854 < \log M \leq 1.096$
$-1.249 \pm 0.028$	$8.623 \pm 0.041$	$1.096 < \log M \leq 1.338$
$-0.869 \pm 0.033$	$8.115 \pm 0.056$	$1.338 < \log M \leq 1.579$
$-0.598 \pm 0.040$	$7.688 \pm 0.077$	$M > 1.579$
$Z = 0.0005$		
$-3.178 \pm 0.023$	$9.777 \pm 0.006$	$\log M \leq 0.130$
$-2.608 \pm 0.021$	$9.703 \pm 0.010$	$0.130 < \log M \leq 0.372$
$-2.415 \pm 0.022$	$9.631 \pm 0.016$	$0.372 < \log M \leq 0.614$
$-2.020 \pm 0.024$	$9.389 \pm 0.024$	$0.614 < \log M \leq 0.856$
$-1.683 \pm 0.027$	$9.101 \pm 0.033$	$0.856 < \log M \leq 1.098$
$-1.247 \pm 0.031$	$8.622 \pm 0.045$	$1.098 < \log M \leq 1.340$
$-0.866 \pm 0.036$	$8.111 \pm 0.062$	$1.340 < \log M \leq 1.582$
$-0.596 \pm 0.044$	$7.685 \pm 0.086$	$\log M > 1.582$
$Z = 0.001$		
$-3.174 \pm 0.026$	$9.797 \pm 0.006$	$\log M \leq 0.135$
$-2.579 \pm 0.024$	$9.716 \pm 0.012$	$0.135 < \log M \leq 0.377$
$-2.466 \pm 0.025$	$9.674 \pm 0.019$	$0.377 < \log M \leq 0.618$
$-2.020 \pm 0.027$	$9.398 \pm 0.027$	$0.618 < \log M \leq 0.860$
$-1.692 \pm 0.030$	$9.116 \pm 0.037$	$0.860 < \log M \leq 1.101$
$1.249 \pm 0.035$	$8.628 \pm 0.051$	$1.101 < \log M \leq 1.342$
$0.868 \pm 0.041$	$8.117 \pm 0.070$	$1.342 < \log M \leq 1.584$
$-0.599 \pm 0.050$	$7.691 \pm 0.097$	$\log M > 1.584$
$Z = 0.003$		
$-3.209 \pm 0.032$	$9.862 \pm 0.008$	$\log M \leq 0.150$
$-2.520 \pm 0.029$	$9.759 \pm 0.015$	$0.150 < \log M \leq 0.385$
$-2.620 \pm 0.030$	$9.797 \pm 0.022$	$0.385 < \log M \leq 0.620$
$-2.091 \pm 0.033$	$9.469 \pm 0.032$	$0.620 < \log M \leq 0.855$
$-1.685 \pm 0.037$	$9.122 \pm 0.045$	$0.855 < \log M \leq 1.090$
$-1.269 \pm 0.042$	$8.669 \pm 0.061$	$1.090 < \log M \leq 1.325$
$-0.937 \pm 0.049$	$8.228 \pm 0.083$	$1.325 < \log M \leq 1.560$
$-0.698 \pm 0.057$	$7.856 \pm 0.110$	$\log M > 1.560$

**Table 10**  
(Continued)

a	b	Validity Range
$Z = 0.006$		
$-3.252 \pm 0.033$	$9.929 \pm 0.009$	$\log M \leq 0.164$
$-2.479 \pm 0.030$	$9.802 \pm 0.015$	$0.164 < \log M \leq 0.392$
$-2.753 \pm 0.031$	$9.910 \pm 0.023$	$0.392 < \log M \leq 0.621$
$-2.194 \pm 0.033$	$9.562 \pm 0.032$	$0.621 < \log M \leq 0.849$
$-1.800 \pm 0.037$	$9.228 \pm 0.044$	$0.849 < \log M \leq 1.077$
$-1.338 \pm 0.043$	$8.730 \pm 0.061$	$1.077 < \log M \leq 1.305$
$-0.898 \pm 0.051$	$8.156 \pm 0.085$	$1.305 < \log M \leq 1.534$
$-0.756 \pm 0.058$	$7.938 \pm 0.110$	$\log M > 1.534$
$Z = 0.008$		
$-3.263 \pm 0.038$	$9.965 \pm 0.010$	$\log M \leq 0.172$
$-2.485 \pm 0.034$	$9.830 \pm 0.017$	$0.172 < \log M \leq 0.398$
$-2.817 \pm 0.034$	$9.962 \pm 0.025$	$0.398 < \log M \leq 0.623$
$-2.226 \pm 0.037$	$9.594 \pm 0.036$	$0.623 < \log M \leq 0.849$
$-1.831 \pm 0.041$	$9.258 \pm 0.049$	$0.849 < \log M \leq 1.074$
$-1.354 \pm 0.048$	$8.746 \pm 0.068$	$1.074 < \log M \leq 1.300$
$-0.908 \pm 0.057$	$8.166 \pm 0.095$	$1.300 < \log M \leq 1.525$
$-0.801 \pm 0.067$	$8.004 \pm 0.125$	$\log M > 1.525$
$Z = 0.010$		
$-3.265 \pm 0.039$	$9.993 \pm 0.011$	$\log M \leq 0.179$
$-2.482 \pm 0.035$	$9.852 \pm 0.018$	$0.179 < \log M \leq 0.403$
$-2.865 \pm 0.035$	$10.007 \pm 0.026$	$0.403 < \log M \leq 0.626$
$-2.272 \pm 0.038$	$9.635 \pm 0.037$	$0.626 < \log M \leq 0.850$
$-1.852 \pm 0.042$	$9.278 \pm 0.051$	$0.850 < \log M \leq 1.073$
$-1.351 \pm 0.049$	$8.740 \pm 0.070$	$1.073 < \log M \leq 1.297$
$-0.955 \pm 0.057$	$8.227 \pm 0.094$	$1.297 < \log M \leq 1.520$
$-0.819 \pm 0.069$	$8.020 \pm 0.129$	$\log M > 1.520$
$Z = 0.020$		
$-3.272 \pm 0.041$	$10.082 \pm 0.012$	$\log M \leq 0.201$
$-2.516 \pm 0.037$	$9.930 \pm 0.020$	$0.201 < \log M \leq 0.418$
$-2.998 \pm 0.037$	$10.131 \pm 0.028$	$0.418 < \log M \leq 0.635$
$-2.406 \pm 0.040$	$9.756 \pm 0.039$	$0.635 < \log M \leq 0.851$
$-1.947 \pm 0.045$	$9.365 \pm 0.053$	$0.851 < \log M \leq 1.068$
$-1.388 \pm 0.052$	$8.767 \pm 0.073$	$1.068 < \log M \leq 1.285$
$-1.028 \pm 0.059$	$8.306 \pm 0.095$	$1.285 < \log M \leq 1.502$
$-0.778 \pm 0.072$	$7.930 \pm 0.132$	$\log M > 1.502$
$Z = 0.030$		
$-3.235 \pm 0.042$	$10.116 \pm 0.013$	$\log M \leq 0.207$
$-2.610 \pm 0.037$	$9.987 \pm 0.019$	$0.207 < \log M \leq 0.418$
$-3.062 \pm 0.037$	$10.176 \pm 0.027$	$0.418 < \log M \leq 0.630$
$-2.483 \pm 0.040$	$9.811 \pm 0.038$	$0.630 < \log M \leq 0.841$
$-2.038 \pm 0.045$	$9.437 \pm 0.052$	$0.841 < \log M \leq 1.052$
$-1.471 \pm 0.051$	$8.841 \pm 0.071$	$1.052 < \log M \leq 1.264$
$-1.163 \pm 0.061$	$8.451 \pm 0.097$	$1.264 < \log M \leq 1.475$
$-0.645 \pm 0.075$	$7.688 \pm 0.136$	$\log M > 1.475$
$Z = 0.035$		
$-3.229 \pm 0.039$	$10.118 \pm 0.012$	$\log M \leq 0.205$
$-2.638 \pm 0.035$	$9.997 \pm 0.018$	$0.205 < \log M \leq 0.414$
$-3.080 \pm 0.034$	$10.180 \pm 0.025$	$0.414 < \log M \leq 0.623$
$-2.537 \pm 0.037$	$9.842 \pm 0.035$	$0.623 < \log M \leq 0.832$
$-2.074 \pm 0.041$	$9.457 \pm 0.047$	$0.832 < \log M \leq 1.041$
$-1.487 \pm 0.048$	$8.845 \pm 0.065$	$1.041 < \log M \leq 1.250$
$-1.166 \pm 0.056$	$8.444 \pm 0.088$	$1.250 < \log M \leq 1.459$



**Table 10**  
(Continued)

a	b	Validity Range
$-0.695 \pm 0.068$	$7.757 \pm 0.122$	$\log M > 1.459$
$Z = 0.039$		
$-3.226 \pm 0.038$	$10.120 \pm 0.011$	$\log M \leq 0.203$
$-2.657 \pm 0.034$	$10.004 \pm 0.017$	$0.203 < \log M \leq 0.411$
$-3.096 \pm 0.033$	$10.184 \pm 0.024$	$0.411 < \log M \leq 0.618$
$-2.576 \pm 0.036$	$9.863 \pm 0.033$	$0.618 < \log M \leq 0.825$
$-2.099 \pm 0.040$	$9.469 \pm 0.045$	$0.825 < \log M \leq 1.033$
$-1.516 \pm 0.046$	$8.867 \pm 0.062$	$1.033 < \log M \leq 1.240$
$-1.185 \pm 0.054$	$8.457 \pm 0.084$	$1.240 < \log M \leq 1.447$
$-0.700 \pm 0.066$	$7.756 \pm 0.117$	$\log M > 1.447$

**Table 11**

Fitting Equations of the Relation between the Relative Long-period Variable Phase Duration ( $\delta t/t$  where  $t$  is the Age and  $\delta t$  is the Long-period Variable Phase Duration) and Birth Mass,  $\log(\delta t/t) = D + \sum_{i=1}^4 a_i \exp[-(\log M[M_\odot] - b_i)^2 / c_i^2]$

$D$	$i$	$a$	$b$	$c$
$Z = 0.0003$				
$-6.926$	1	3.848	0.620	0.876
	2	0.513	0.248	0.070
	3	4.833	1.821	0.432
	4	342.189	-1.779	0.009
$Z = 0.0005$				
$-5.054$	1	1.810	0.586	0.211
	2	1.882	0.248	0.159
	3	3.526	1.666	0.271
	4	1.496	1.169	0.197
$Z = 0.001$				
$-4.570$	1	1.336	0.589	0.166
	2	0.949	1.148	0.099
	3	3.481	1.513	0.252
	4	1.610	0.265	0.160
$Z = 0.003$				
$-5.323$	1	1.531	1.826	0.151
	2	3.421	1.337	0.405
	3	2.566	0.306	0.290
	4	1.288	0.647	0.127
$Z = 0.006$				
$-5.809$	1	3.149	0.336	0.366
	2	4.238	1.290	0.444
	3	0.676	0.662	0.095
	4	2.149	1.757	0.116
$Z = 0.008$				
$-10.000$	1	7.386	0.375	0.676
	2	0.637	0.695	0.088
	3	7.380	1.538	0.289
	4	5.073	1.133	0.261
$Z = 0.010$				
$-8.225$	1	3.056	1.062	0.209
	2	0.697	0.711	0.095
	3	6.275	1.444	0.333

**Table 11**  
(Continued)

$D$	$i$	$a$	$b$	$c$
	4	5.593	0.385	0.598
$Z = 0.020$				
−5.542	1	4.273	1.216	0.584
	2	2.255	0.304	0.354
	3	−1.954	0.881	0.091
	4	0.225	0.450	0.044
$Z = 0.030$				
−6.646	1	5.349	1.208	0.580
	2	0.966	0.992	0.037
	3	−2.628	0.918	0.094
	4	3.189	0.324	0.435
$Z = 0.035$				
−5.497	1	−3.283	0.887	0.102
	2	2.571	0.381	0.343
	3	1.719	0.851	0.223
	4	4.088	1.248	0.433
$Z = 0.039$				
−5.321	1	−2.402	0.884	0.052
	2	2.247	0.373	0.308
	3	0.604	0.688	0.092
	4	4.053	1.192	0.468

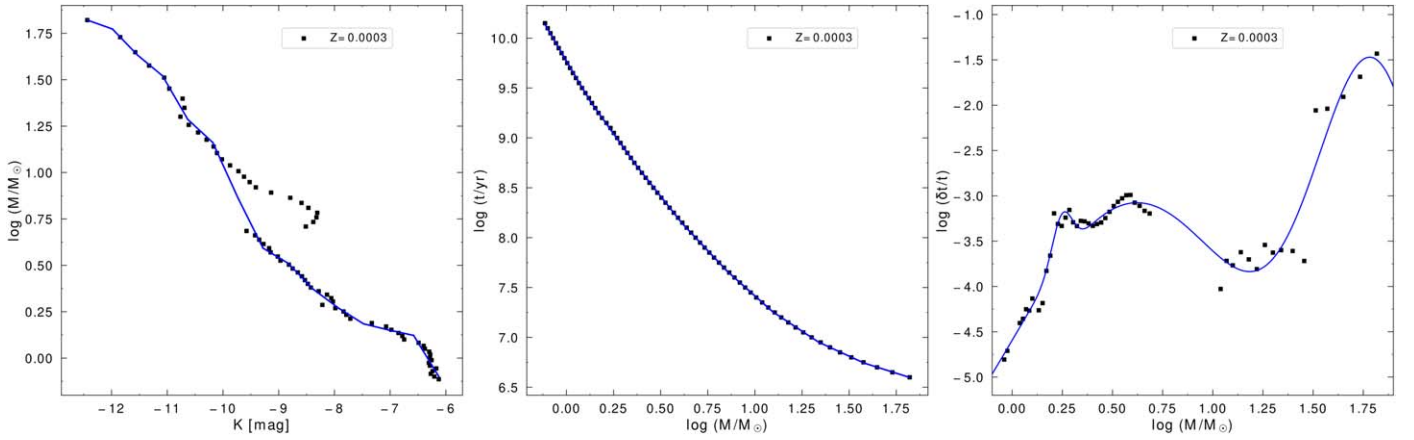


**Figure 17.** Left panel: the mass–luminosity relation in the  $Ks$  band for a metallicity of  $Z = 0.0003$ . The solid lines are linear spline fits, for the case in which the function is interpolated across the super-AGB phase to massive RSGs, i.e., for  $0.7 < \log(M/M_\odot) < 1-1.1$ . Middle panel: the mass–age relation for a metallicity of  $Z = 0.0003$  along with linear spline fits. Right panel: the mass–LPV phase duration relation for the same metallicity, where the points show the ratio of LPV phase duration to age vs. mass; the solid lines are multi-Gaussian fits. The complete figure set (11 images) is available in the online journal.

(The complete figure set (11 images) is available in the [online article](#).)

### A.2. Probability Function Details

To determine the probability function, we use the data from Rejkuba et al. (2003a), which are classified into three categories. They are marked with “circle,” “cross,” and “triangle” points corresponding to simulated variable stars, which are considered as a function of amplitude regardless of their magnitudes for all the stars, simulated variable stars with

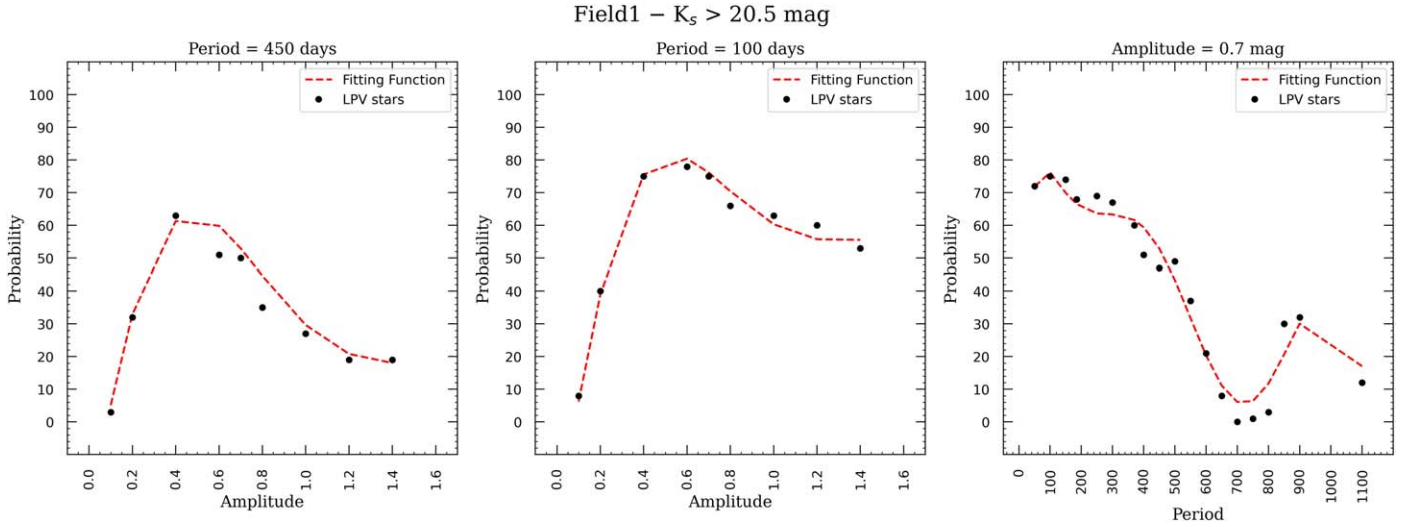
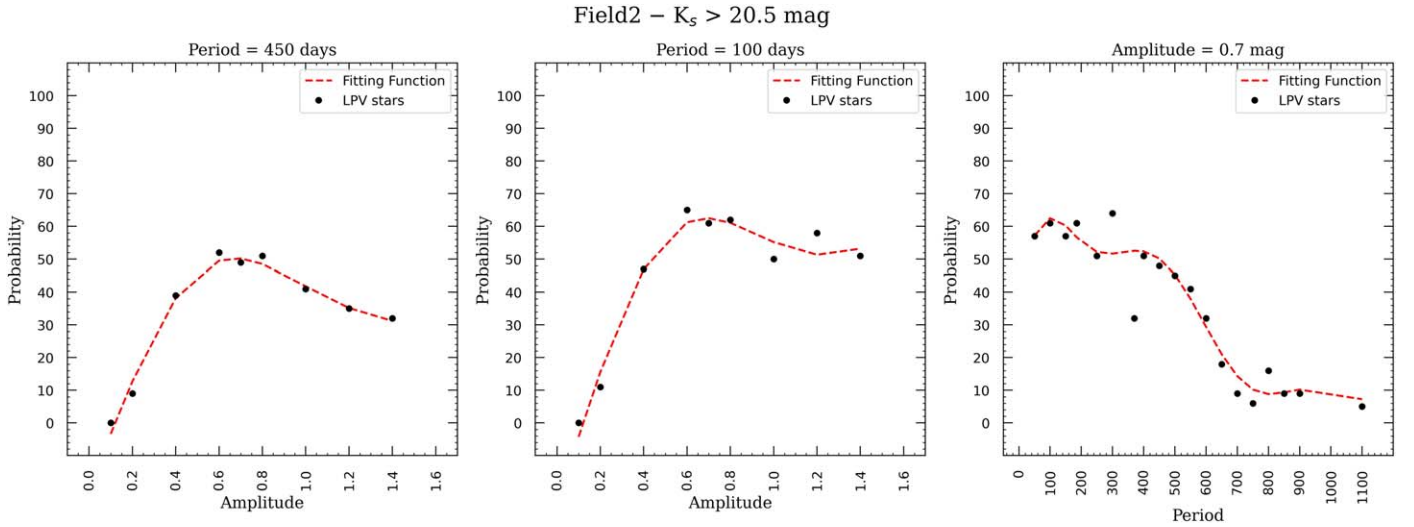
$Ks > 20.5$  mag, and the ones brighter than  $Ks < 20$  mag, respectively. They are all presented in Section 6 of Rejkuba et al. (2003a) and Figures 12 and 14. These simulated variable stars have been reproduced in terms of their amplitude, period, and mean magnitude based on the catalog.

The final probability function of simulated variable stars is parameterized in Equation (7) whose coefficients are mentioned in Table 12 for both Field 1 and Field 2.

**Table 12**

Coefficient of the Probability Function of Field 1 and Field 2 for Simulated Variable Stars by Considering the Amplitude Regardless of their Magnitude, Equation (7)

$N$	Symbol	Field 1	Field 2
		Coefficient	Coefficient
1	$\alpha_1$	-16.231	-6.348
2	$\alpha_2$	17.628	7.278
3	$\alpha_3$	$-8.986 \times 10^{-2}$	$7.588 \times 10^{-2}$
4	$\beta$	1.227	$3.364 \times 10^{-1}$
5	$\eta$	$9.733 \times 10^{-1}$	2.991
6	$\gamma_1$	$6.483 \times 10^{-1}$	2.412
7	$\gamma_2$	$-6.427 \times 10^{-3}$	$-2.507 \times 10^{-2}$
8	$\gamma_3$	$3.063 \times 10^{-7}$	$1.178 \times 10^{-4}$
9	$\gamma_4$	$-7.559 \times 10^{-8}$	$-2.820 \times 10^{-7}$
10	$\gamma_5$	$9.749 \times 10^{-11}$	$3.545 \times 10^{-10}$
11	$\gamma_6$	$-6.228 \times 10^{-14}$	$-2.230 \times 10^{-13}$
12	$\gamma_7$	$1.555 \times 10^{-17}$	$5.536 \times 10^{-17}$
13	$\delta_1$	$-2.014 \times 10^4$	$-4.106 \times 10^4$
14	$\delta_2$	$-1.000 \times 10^6$	$6.205 \times 10^6$
15	$\delta_3$	1.000	1.000
16	$\delta_4$	$3.434 \times 10^3$	$1.153 \times 10^2$

**Figure 18.** The result of fitting the probability function for simulated variable stars with  $K_s > 20.5$  mag in Field 1.**Figure 19.** The result of fitting the probability function for simulated variable stars with  $K_s > 20.5$  mag in Field 2.



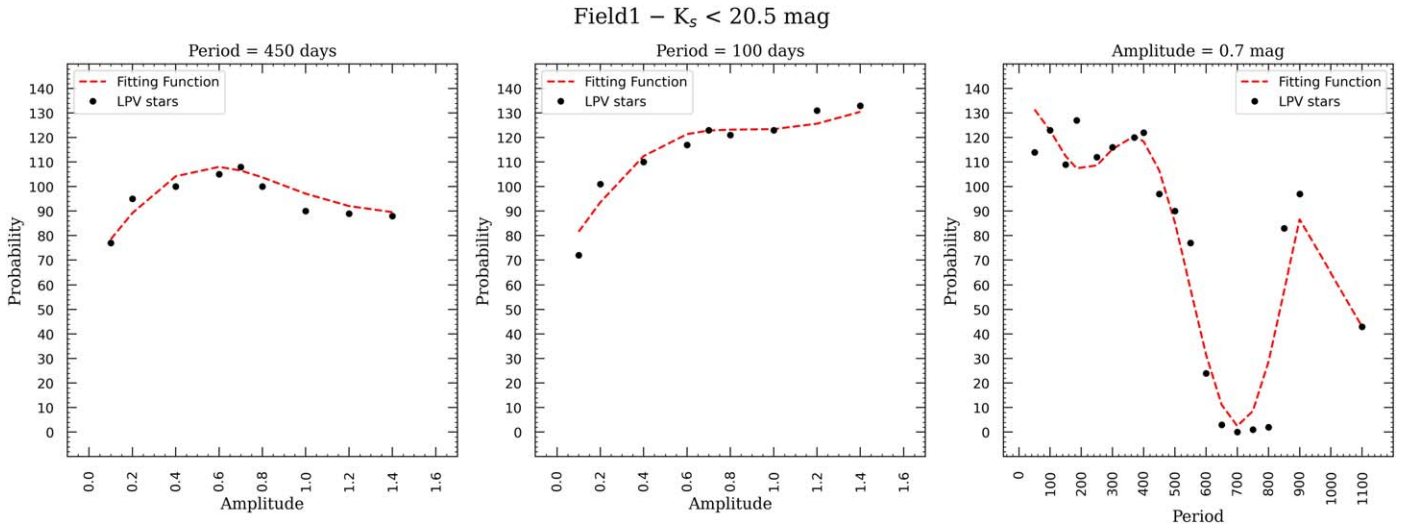


**Figure 20.** The result of fitting the probability function for simulated variable stars with  $K_s < 20.5$  mag in Field 1.

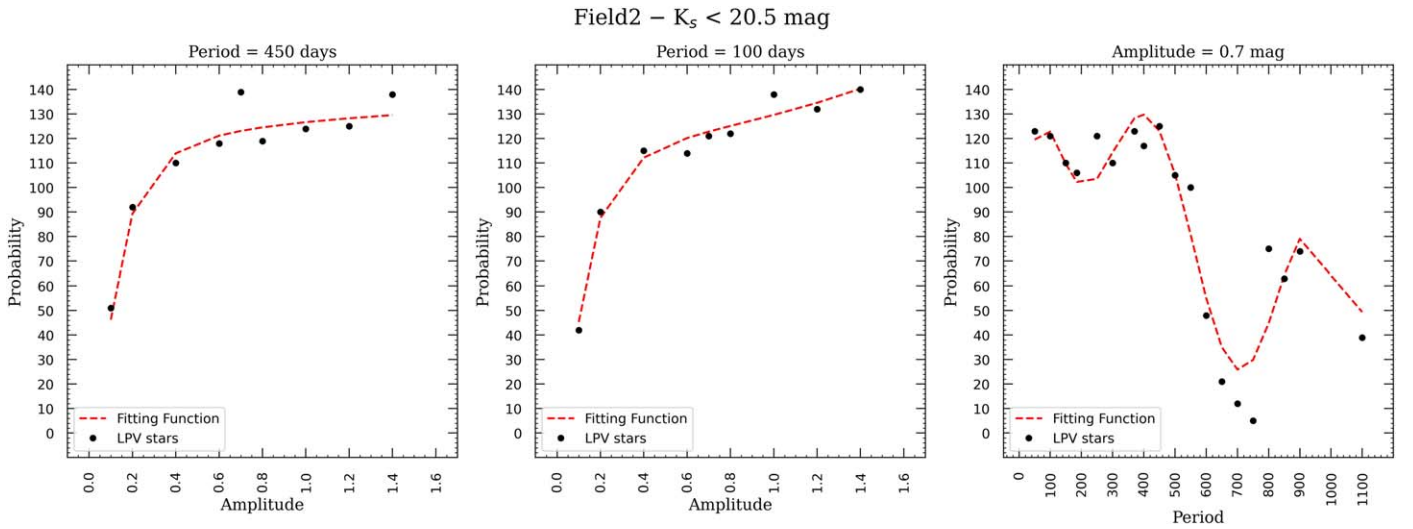


**Figure 21.** The result of fitting the probability function for simulated variable stars with  $K_s < 20.5$  mag in Field 2.

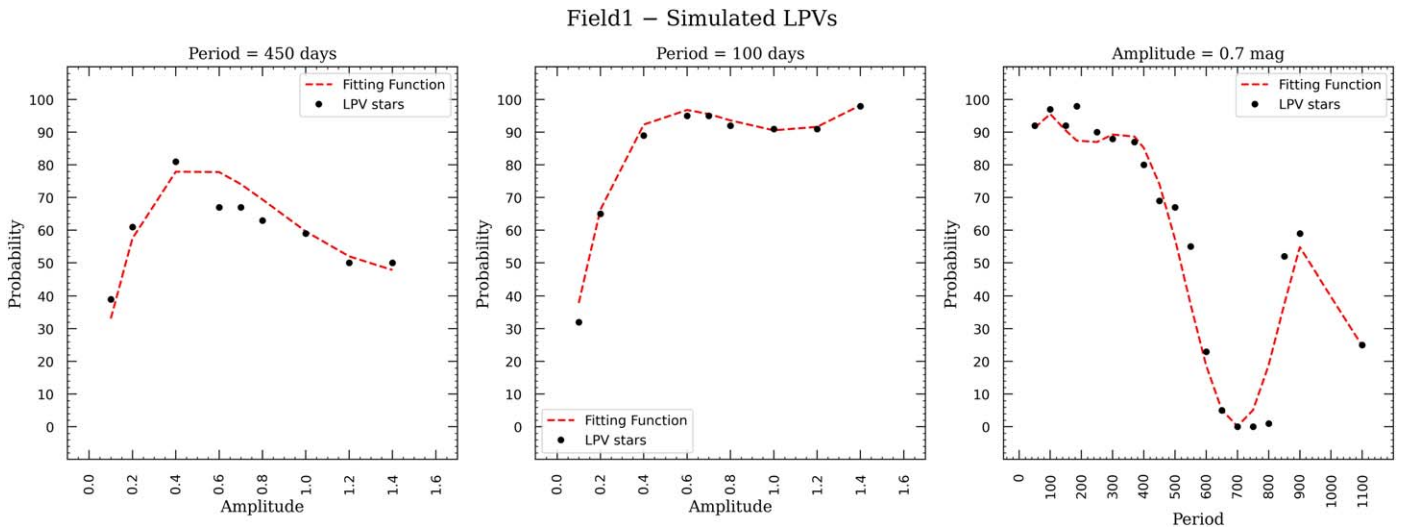


**Figure 22.** The result of fitting the probability function for the simulated LPV stars by considering the amplitude regardless of their magnitude of Field 1.

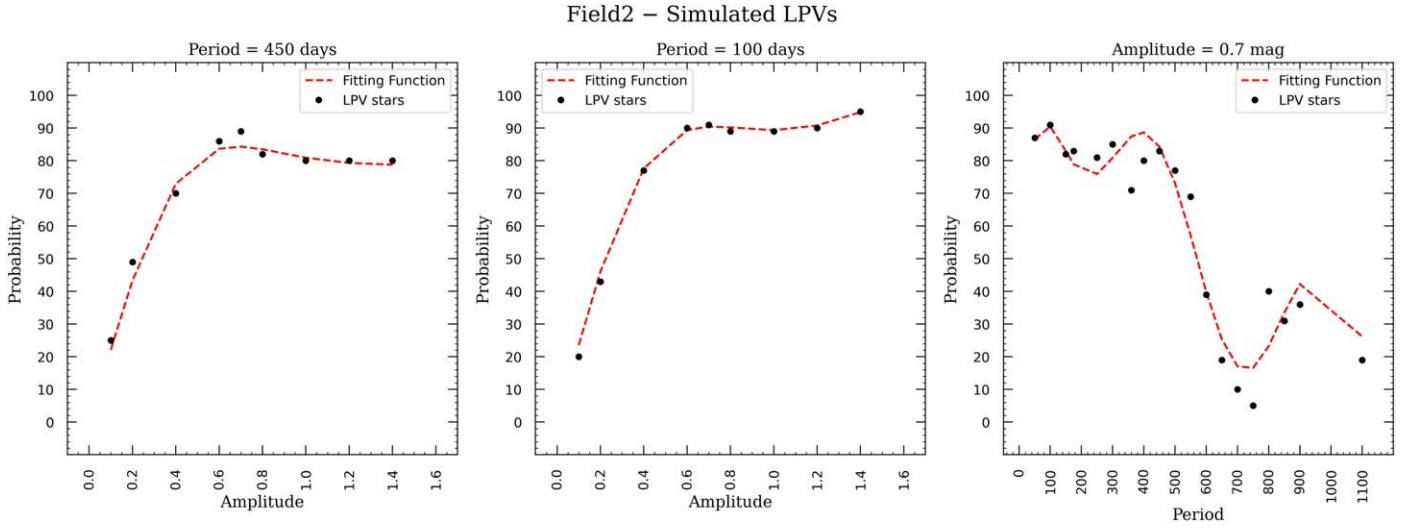


**Figure 23.** The result of fitting probability function for the simulated LPV stars by considering the amplitude regardless of their magnitude of Field 2.

To accomplish this, we encountered a drop after reaching the peak for the simulated LPV stars fainter than  $K_s = 20.5$  mag. Two reasons were mentioned in Rejkuba et al. (2003a), which are related increased photometric errors and the difference in completeness limits for the  $H$ ,  $J_s$ , and  $K_s$  bands. Fainter stars have a lower completeness limit, as the fainter parts of their light curve would not have been detected.

The plots which depict the accuracy of fitting probability functions are presented in Figures 18–23 for Field 1 and Field 2.

### A.3. Overview Plots of the Star Formation Rate

For a detailed overview of the SFR, it is plotted separately for each metallicity of Fields 1 and 2 in Figures 24 and 25, respectively.

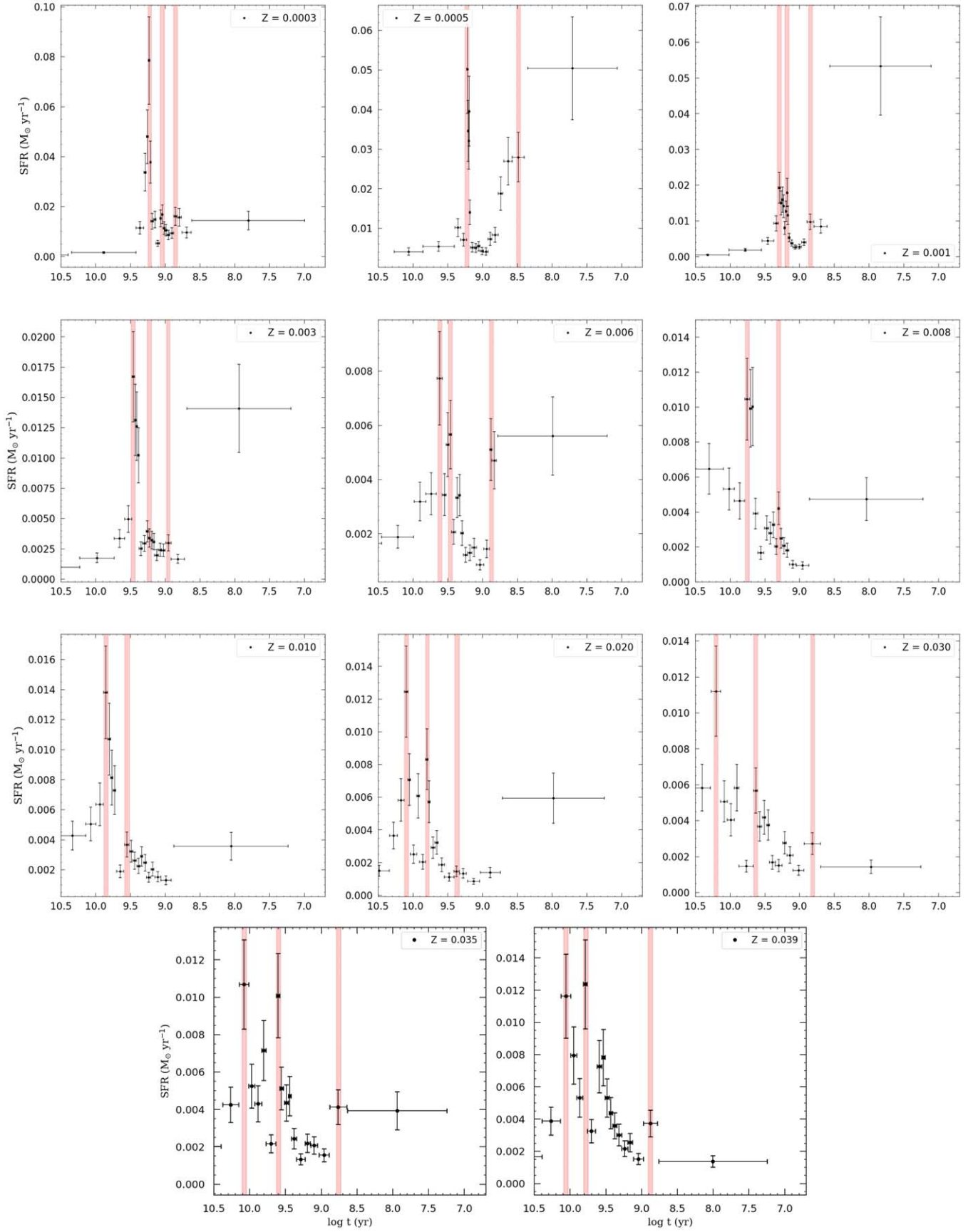



**Figure 24.** The SFRs of Field 1 for different metallicities in separate panels after applying the probability function. Each panel is scaled to one and the red regions are the desired epochs of the SFR. The highlighted regions represent the peaks of star formation during the major epochs.



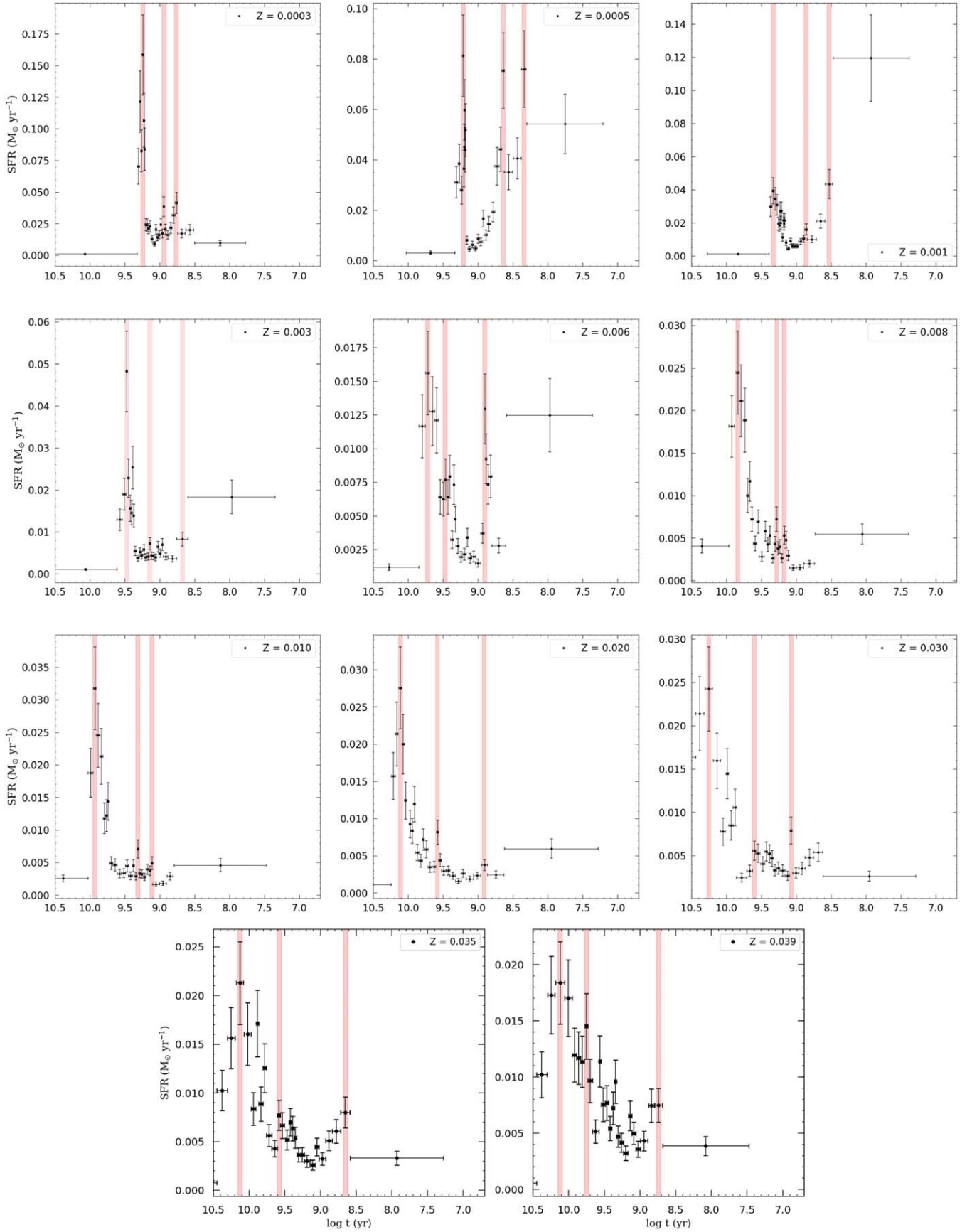


**Figure 25.** The SFRs of Field 2 for different metallicities in separate panels after applying the probability function. Each panel is scaled to one and the red regions are the desired epochs of the SFR. The highlighted regions represent the peaks of star formation during the major epochs.

## ORCID iDs

Atefeh Javadi  <https://orcid.org/0000-0001-8392-6754>  
 Jacco Th. van Loon  <https://orcid.org/0000-0002-1272-3017>  
 Roya H. Golshan  <https://orcid.org/0000-0003-1993-2302>  
 Elham Saremi  <https://orcid.org/0000-0002-5075-1764>  
 Maryam Saberi  <https://orcid.org/0000-0001-7353-9101>

## References

- Abromowitz, M., & Stegun, I. A. 1972, *Handbook of Mathematical Functions* (New York: Dover)
- Auld, R., Smith, M. W. L., Bendo, G., et al. 2012, *MNRAS*, **420**, 1882
- Baade, W., & Minkowski, R. 1954, *ApJ*, **119**, 215
- Barnes, J. E. 1992, *ApJ*, **393**, 484
- Barnes, J. E., & Hernquist, L. 1996, *ApJ*, **471**, 115
- Beasley, M. A., Bridges, T., Peng, E., et al. 2008, *MNRAS*, **386**, 1443
- Best, P. N., & Heckman, T. M. 2012, *MNRAS*, **421**, 1569
- Binney, J. 2004, *MNRAS*, **347**, 1093
- Blanco, V. M., Graham, J. A., Lasker, B. M., & Osmer, P. S. 1975, *ApJ*, **198**, L63
- Bournaud, F. 2011, *EAS*, **51**, 107
- Boylan-Kolchin, M., Ma, C.-P., & Quataert, E. 2005, *MNRAS*, **362**, 184
- Brown, A. G. A., Vallenari, A., Prusti, T., et al. 2021, *A&A*, **649**, A1
- Charmandaris, V., Combes, F., & van der Hulst, J. M. 2000, *A&A*, **356**, L1
- Ciotti, L., & Ostriker, J. P. 1997, *ApJ*, **487**, L105
- Clarke, D. A., Burns, J. O., & Norman, M. L. 1992, *ApJ*, **395**, 444
- Combes, F., & Charmandaris, V. 1999, *ASP Conf. Ser. Galaxy Dynamics*, 182, ed. D. R. Merritt, M. Valuri, & J. A. Sellwood (San Francisco, CA: ASP), 489
- Cox, T. J., Dutta, S. N., Di Matteo, T., et al. 2006, *ApJ*, **650**, 791
- Crnojević, D., Sand, D. J., Caldwell, N., et al. 2014, *ApJ*, **795**, L35
- Crnojević, D., Sand, D. J., Spekkens, K., et al. 2016, *ApJ*, **823**, 19
- Crockett, R. M., Shabala, S. S., Kaviraj, S., et al. 2012, *MNRAS*, **421**, 1603
- Dekel, A., & Birnboim, Y. 2006, *MNRAS*, **368**, 2
- Dekel, A., Birnboim, Y., Engel, G., et al. 2009, *Natur*, **457**, 451
- Dolphin, A. E. 2002, *MNRAS*, **332**, 91
- D'Souza, R., & Bell, E. F. 2018, *MNRAS*, **474**, 5300
- Dubinski, J., Mihos, J. C., & Hernquist, L. 1996, *ApJ*, **462**, 576
- Dupraz, C., & Combes, F. 1987, *A&A*, **185**, L1
- Emonts, B. H. C., Norris, R. P., Feain, I., et al. 2014, *MNRAS*, **438**, 2898
- Fassett, C. I., & Graham, J. A. 2000, *ApJ*, **538**, 594
- Feain, I. J., Cornwell, T. J., Ekers, R. D., et al. 2011, *ApJ*, **740**, 17
- Fragile, P. C., Murray, S. D., Anninos, P., & van Breugel, W. 2004, *ApJ*, **604**, 74
- Fraser, O. J., Hawley, S. L., Cook, K. H., & Keller, S. C. 2005, *AJ*, **129**, 768
- Fraser, O. J., Hawley, S. L., & Cook, K. H. 2008, *AJ*, **136**, 1242
- Gaibler, V., Khochfar, S., Krause, M., & Silk, J. 2012, *MNRAS*, **425**, 438
- Girardi, L., Groenewegen, M. A. T., Hatziminaoglou, E., & da Costa, L. 2005, *A&A*, **436**, 895
- Graham, J. A. 1979, *ApJ*, **232**, 60
- Graham, J. A., & Price, R. M. 1981, *ApJ*, **247**, 813
- Guo, Q., White, S., Boylan-Kolchin, M., et al. 2011, *MNRAS*, **413**, 101
- Hamedani Golshan, R., Javadi, A., van Loon, J. T., et al. 2017, *MNRAS*, **466**, 1764
- Hardcastle, M. J., Cheung, C. C., Feain, I. J., & Stawarz, L. 2009, *MNRAS*, **393**, 1041
- Harris, G. L. H. 2010, *PASA*, **27**, 475
- Harris, G. L. H., Harris, W. E., & Poole, G. B. 1999, *AJ*, **117**, 855
- Hashemi, S. A., Javadi, A., & van Loon, J. T. 2019, *MNRAS*, **483**, 4751
- Hernandez, S., Larsen, S., Trager, S., et al. 2018, *MNRAS*, **476**, 5189
- Hernquist, L. 1993, *ApJS*, **86**, 389
- Holtzman, J. A., Gallagher, J. S., Cole, A. A., et al. 1999, *AJ*, **118**, 2262
- Israel, F. 1998, *A&ARv*, **8**, 237
- Iverson, R. J., Smail, I., Amblard, A., et al. 2012, *MNRAS*, **425**, 1320
- Javadi, A., Saberi, M., van Loon, J. T., et al. 2015, *MNRAS*, **447**, 3973
- Javadi, A., van Loon, J. T., Khosroshahi, H., & Mirtorabi, M. T. 2013, *MNRAS*, **432**, 2824
- Javadi, A., van Loon, J. T., Khosroshahi, H., et al. 2017, *MNRAS*, **464**, 2103
- Javadi, A., van Loon, J. T., & Mirtorabi, M. T. 2011a, *MNRAS*, **411**, 263
- Javadi, A., van Loon, J. T., & Mirtorabi, M. T. 2011b, *MNRAS*, **414**, 3394
- Javadi, A., van Loon, J. T., & Mirtorabi, M. T. 2011c, in *ASP Conf. Ser.* 445, *Why Galaxies Care About AGB Stars II: Shining Examples and Common Inhabitants*, ed. F. Kerschbaum, T. Lebzelter, & R. F. Wing (San Francisco, CA: ASP), 497
- Joseph, P., Sreekumar, P., Stalin, C. S., et al. 2022, *MNRAS*, **516**, 2300
- Karachentsev, I. D. 2005, *AJ*, **129**, 178
- Kaviraj, S., Devriendt, J. E. G., Ferreras, I., & Yi, S. K. 2005, *MNRAS*, **360**, 60
- Kroupa, P. 2001, *MNRAS*, **322**, 231
- Leisenring, J. M., Kemper, F., & Sloan, G. C. 2008, *ApJ*, **681**, 1557
- Ma, C., Arias, E. F., Eubanks, T. M., et al. 1998, *AJ*, **116**, 516
- Malin, D. F., Quinn, P. J., & Graham, J. A. 1983, *ApJ*, **272**, L5
- Maraston, C. 2005, *MNRAS*, **362**, 799
- Maraston, C., Daddi, E., Renzini, A., et al. 2006, *ApJ*, **652**, 85
- Marigo, P., Girardi, L., Bressan, A., et al. 2008, *A&A*, **482**, 883
- Marigo, P., Girardi, L., Bressan, A., et al. 2017, *ApJ*, **835**, 77
- McKinley, B., Briggs, F., Gaensler, B. M., et al. 2013, *MNRAS*, **436**, 1286
- Mo, H., Van den Bosch, F., & White, S. D. M. 2010, *Galaxy formation and evolution* (Cambridge: Cambridge Univ. Press)
- Morgan, W. W. 1958, *PASP*, **70**, 364
- Morganti, R. 2010, *PASA*, **27**, 463
- Morganti, R., Killeen, N. E. B., Ekers, R. D., & Oosterloo, T. A. 1999, *MNRAS*, **307**, 750
- Morganti, R., Robinson, A., Fosbury, R. A. E., et al. 1991, *MNRAS*, **249**, 91
- Mould, J. R., Ridgewell, A., Gallagher, J. S., et al. 2000, *ApJ*, **536**, 266
- Naab, T., & Burkert, A. 2003, *ApJ*, **597**, 893
- Navabi, M., Saremi, E., Javadi, A., et al. 2021, *ApJ*, **910**, 127
- Neff, S. G., Eilek, J. A., & Owen, F. N. 2015, *ApJ*, **802**, 88
- Olsen, K. A. G. 1999, *AJ*, **117**, 2244
- Oosterloo, T., & Morganti, R. 2004, *A&A*, **429**, 469
- Peng, E. W., Ford, H. C., Freeman, K. C., & White, R. L. 2002, *AJ*, **124**, 3144
- Peng, E. W., Ford, H. C., & Freeman, K. C. 2004, *ApJ*, **602**, 705
- Pietrinferni, A., Cassisi, S., Salaris, M., & Castelli, F. 2004, *ApJ*, **612**, 168
- Pietrinferni, A., et al. 2021, *ApJ*, **908**, 102
- Quinn, P. J. 1984, *ApJ*, **279**, 596
- Rejkuba, M. 2004b, *A&A*, **413**, 903
- Rejkuba, M., Greggio, L., Harris, W. E., et al. 2005, *ApJ*, **631**, 262
- Rejkuba, M., Greggio, L., & Zoccali, M. 2004a, *A&A*, **415**, 915
- Rejkuba, M., Harris, W. E., Greggio, L., & Harris, G. L. H. 2011, *A&A*, **526**, A123
- Rejkuba, M., Harris, W. E., Greggio, L., et al. 2014, *ApJ*, **791**, L2
- Rejkuba, M., Harris, W. E., Greggio, L., et al. 2022, *A&A*, **657**, A41
- Rejkuba, M., Minniti, D., Courbin, F., & Silva, D. 2002, *ApJ*, **564**, 688
- Rejkuba, M., Minniti, D., Silva, D., & Bedding, T. 2001, *A&A*, **379**, 781
- Rejkuba, M., Minniti, D., Silva, D., & Bedding, T. 2003b, *A&A*, **411**, 351
- Rejkuba, M., Minniti, D., & Silva, D. 2003a, *A&A*, **406**, 75
- Rezaei, K. S., Javadi, A., Khosroshahi, H., & van Loon, J. Th. 2014, *MNRAS*, **445**, 2214
- Ruiz-Lara, T., Pérez, I., Gallart, C., et al. 2015, *A&A*, **583**, A60
- Salomé, Q., Salomé, P., Combes, F., & Hamer, S. 2016a, *A&A*, **595**, A65
- Salomé, Q., Salomé, P., Combes, F., et al. 2016b, *A&A*, **586**, A45
- Salomé, Q., Salomé, P., Miville-Deschênes, M. A., et al. 2017, *A&A*, **608**, A98
- Sánchez Almeida, J., Elmegreen, B. G., Muñoz-Tuñón, C., & Elmegreen, D. M. 2014, *A&ARv*, **22**, 71
- Santoro, F., Oonk, J. B. R., Morganti, R., et al. 2015a, *A&A*, **574**, A89
- Santoro, F., Oonk, J. B. R., Morganti, R., et al. 2015b, *A&A*, **575**, L4
- Santoro, F., Oonk, J. B. R., Morganti, R., et al. 2016, *A&A*, **590**, A37
- Saremi, E., Javadi, A., Navabi, M., et al. 2021, *ApJ*, **923**, 164
- Saremi, E., Javadi, A., van Loon, J. T., et al. 2020, *ApJ*, **894**, 135
- Saxton, C. J., Sutherland, R. S., & Bicknell, G. V. 2001, *ApJ*, **563**, 103
- Schawinski, K., Thomas, G., Sarzi, M., et al. 2007, *MNRAS*, **382**, 1415
- Schiminovich, D., van Gorkom, J. H., van der Hulst, J. M., & Kasow, S. 1994, *ApJ*, **423**, L101
- Schreier, E. J., Burns, J. O., & Feigelson, E. D. 1981, *ApJ*, **251**, 523
- Siess, L. 2007, *A&A*, **476**, 893
- Sijacki, D., Springel, V., di Matteo, T., & Hernquist, L. 2007, *MNRAS*, **380**, 877
- Silk, J. 2005, *MNRAS*, **364**, 1337
- Silk, J., & Rees, M. J. 1998, *A&A*, **331**, L1
- Soszyński, I., Udalski, A., Szymański, M. K., et al. 2009, *AcA*, **59**, 239
- Sparke, L. S. 1996, *ApJ*, **473**, 810
- Springel, V., Di Matteo, T., & Hernquist, L. 2005, *ApJ*, **620**, L79
- Springel, V., & White, S. D. M. 1999, *MNRAS*, **307**, 162
- Tolstoy, E., & Saha, A. 1996, *ApJ*, **462**, 672
- Tubbs, A. D. 1980, *ApJ*, **241**, 969
- van den Bergh, S. 1990, *ApJ*, **348**, 57
- van der Marel, R. P., Fardal, M. A., Sohn, S. T., et al. 2019, *ApJ*, **872**, 14

- van Loon, J. Th., Cioni, M.-R. L., Zijlstra, A. A., & Loup, C. 2005, [A&A](#), **438**, 273
- van Loon, J. Th., Groenewegen, M. A. T., & de Koter, A. 1999, [A&A](#), **351**, 559
- Vassiliadis, E., & Wood, P. R. 1993, [ApJ](#), **413**, 641
- Wang, J., Hammer, F., Rejkuba, M., et al. 2020, [MNRAS](#), **498**, 2766
- Weil, M. L., & Hernquist, L. 1993, [ApJ](#), **405**, 142
- Whitelock, P. A., Feast, M. W., van Loon, J. T., & Zijlstra, A. A. 2003, [MNRAS](#), **342**, 86
- Wood, P. R. 2000, [PASA](#), **17**, 18
- Woodley, K. A., Harris, W. E., Puzia, T. H., et al. 2010, [ApJ](#), **708**, 1335
- Yang, M., & Jiang, B. W. 2012, [ApJ](#), **754**, 35
- Yi, S. K., Peng, E., Ford, H., et al. 2004, [MNRAS](#), **349**, 1493